

The role of nanoparticles in mediating element deposition and transport at hydrothermal vents

Amy Gartman^{a,*}, Alyssa J. Findlay^{b,1}, Mark Hannington^{c,d},
Dieter Garbe-Schönberg^e, John W. Jamieson^f, Tom Kwasnitschka^c

^a US Geological Survey, PCMSC, 2885 Mission St., Santa Cruz, CA 95060, USA

^b Department of Geological and Environmental Sciences, Ben-Gurion University of the Negev, Beer Sheva, Israel

^c GEOMAR – Helmholtz Centre for Ocean Research Kiel, 1-3 Wischhofstr., 24148 Kiel, Germany

^d Department of Earth Sciences, University of Ottawa, Ottawa, ON K1N 6N5, Canada

^e Institute of Geosciences, Kiel University, Ludewig-Meyn-Strasse 10, 24118 Kiel, Germany

^f Department of Earth Sciences, Memorial University of Newfoundland, St. John's, NL A1B 3X5, Canada

Received 13 December 2018; accepted in revised form 28 June 2019; Available online 8 July 2019

Abstract

Precipitation processes in hydrothermal fluids exert a primary control on the eventual distribution of elements, whether that sink is in the seafloor, hydrothermal chimneys, near-field metalliferous sediments, or more distal in the ocean basin. Recent studies demonstrating abundant nanoparticles in hydrothermal fluids raise questions as to the importance of these nanoparticles relative to macro minerals, as well as the fate of such particles in hydrothermal systems. Here we evaluate the particle geochemistry of black smoker fluids from Niuia South vent field, including nanoparticles and macro minerals, in order to consider how the processes of mineral precipitation affect mineral size and morphology, and how this mineral precipitation may dictate element sinks as hydrothermal fluids begin to mix with seawater. We find that the Niuia vent fluids are dominated by sulfide and sulfate minerals, with the mineralogy of major and minor minerals changing with temperature, degree of mixing with seawater and rate of precipitation. The majority of particles are submicron in size, and sulfide minerals become larger and exhibit more crystalline morphology with increasing seawater content in the fluids. Minor minerals include gold and bismuth tellurides, and nanoparticulate chalcopyrite and nano-zinc sulfide occur. These findings are consistent with major mineral classes and precipitation processes observed in other systems, while providing further insight into the details of mineral precipitation at Niuia including the separate and combined influences of boiling, mixing and cooling during hydrothermal fluid transport and initial interactions with seawater. This work demonstrates that boiling and rapid mixing encourages the formation of nanoparticles, whereas conductive cooling encourages particle growth. Further, these data demonstrate that the possible influence of nanoparticles in hydrothermal systems are not restricted to enhancing element transport, but may also include restricting mineral growth and affecting physicochemical properties of hydrothermal chimneys.

Published by Elsevier Ltd. This is an open access article under the CC BY-NC-ND license (<http://creativecommons.org/licenses/by-nc-nd/4.0/>).

Keywords: hydrothermal; nanoparticles; precipitation

* Corresponding author.

E-mail addresses: agartman@usgs.gov (A. Gartman), afindlay@bios.au.dk (A.J. Findlay), mhannington@geomar.de (M. Hannington), dgs@gpi.uni-kiel.de (D. Garbe-Schönberg), jjamieson@mun.ca (J.W. Jamieson), tkwasnitschka@geomar.de (T. Kwasnitschka).

¹ Present address: Center for Geomicrobiology, Department of Biological Sciences, Aarhus University, Aarhus C, Denmark.

1. INTRODUCTION

The mineralogy, size, and fate of particles formed at the interface of hydrothermal fluids and ocean water has been of interest since the first observations of active hydrothermal vents. Early research recognized that different particle plumes formed at seafloor chimneys, with “black smokers” indicating higher temperature and comprised mainly of sulfide minerals, and “white smokers” forming at lower temperature and composed of amorphous silica, barite, and pyrite (Haymon and Kastner, 1981) or zinc and calcium rich particles (James and Elderfield, 1996). Since this initial discovery, the diversity of hydrothermal systems and mineralization processes continues to expand. A variety of minerals have been identified in hydrothermal plumes including various metal sulfides (e.g., chalcopyrite, pyrite, sphalerite, pyrrhotite), barite, iron oxides, elemental sulfur, and silicates, in sizes from <2 to 100 μm (Feely et al., 1987). Although the general trend from a dominance of sulfide minerals near the vents, to oxide minerals farther from the vents has long been a paradigm, a detailed understanding of where in the hydrothermal system or plume such particles form, the diversity of such particles, and their residence times is still emerging. Empirical description and quantification of sub-micron and nano-sized minerals in hydrothermal plumes is fairly recent (Yücel et al., 2011; Gartman et al., 2014), although significant stability and dispersal for small sulfide minerals (Feely et al., 1987), and the presence of copper containing colloids has long been suggested (James and Elderfield, 1996).

The dynamic nature of hydrothermal plumes and the rapid cooling of hydrothermal fluid upon emission into seawater also results in enhanced microbial activity and organic matter entrainment. As a result, almost all studies of hydrothermal fluid-borne minerals focus on particles in the rising or neutrally buoyant plume, rather than in the high-temperature fluids. Breier et al. (2012) observed a range of minerals, from <2 nm to >10 μm in diameter, embedded in organic aggregates within a plume above EPR 9°50'N, and noted that the mineralogy was inconsistent with thermodynamic models, indicating the complexity of particle formation reactions in hydrothermal systems. Previous work has performed couple *in-situ* filtration to synchrotron-based techniques to examine microbial interactions, carbon geochemistry, and crystalline and poorly crystalline minerals (Toner et al. (2016) and has demonstrated that the metals interacting with organic material in the rising hydrothermal plume need not be mineral associated (e.g., Toner et al., 2009; Sander and Koschinsky, 2011). Kleint et al. (2016) recently demonstrated via voltammetric analysis that only 1–12% of Fe in the rising hydrothermal plume is chemically labile. These studies investigate element pools that have avoided immediate settling, are strongly associated with organic material, and are therefore a step removed from initial hydrothermal emissions but are more applicable to potential basin (and global) element transport.

In contrast to plume studies, an examination of the particles in high-temperature fluids allows us to constrain the initial conditions of precipitation in the vent fluid with

variable amounts of seawater entrainment and little to no biological influence. It has been demonstrated that abundant nanoparticles are emitted in high-temperature hydrothermal fluids (Gartman et al., 2014; Yücel et al., 2011), although knowledge of the factors controlling nanoparticle formation and global transport is just beginning. Iron has been the focus of many recent investigations into hydrothermal plume geochemistry due to its importance as a micronutrient in the surface ocean, but there are many other elements emitted from these systems which are elevated orders of magnitude relative to seawater, transported as particles, and are biologically relevant, and/or of societal interest. The current interest in mining seafloor minerals, including seafloor sulfide deposits and metalliferous sediments, has emphasized the need for quantitative information on the mineralogy, size classes, chemistry, and potential fate of emitted particles.

This study focuses on Niua South, a boiling hydrothermal site on an arc volcano in the Northeast Lau Basin. Previous studies of Niua have discussed mineralogy, which includes abundant sphalerite, chalcopyrite pyrite, barite and anhydrite occurring in low mounds of massive sulfide capped by active chimneys (Jankowski, 2011; Peterkin et al., 2018), conducted detailed mapping of the crater containing the active vents (Kwasnitschka et al., 2016). Previous work has also discussed gas chemistry, and notes that Niua exhibits arc-like characteristics based on fluid helium/carbon ratios (Lupton et al., 2015). Hydrothermal systems on arc volcanoes are typically shallow compared to mid-ocean ridge and back-arc hydrothermal systems, and boiling, which is observed at Niua, is not uncommon (Monecke et al., 2014); prior studies have also observed phase separation either directly or through salinity changes in the resultant fluids in shallow seafloor systems (Stoffers et al., 2006; Schmidt et al., 2017).

At hydrothermal vent sites that are not actively boiling, fluid mixing and cooling are considered to be primary controls on mineral precipitation; these processes co-occur as hydrothermal fluids are mixed into cold seawater. Based on a combination of thermodynamic modeling and particle analyses from several hydrothermal sites along the Mid-Atlantic Ridge, Klevenz et al. (2011) suggested that, mixing provided a more important control on particle formation than cooling. However, the number of studies examining these processes separately is limited, and the relative importance of each process will vary between hydrothermal systems.

Here we examine particle geochemistry of hydrothermal fluids from Niua South vent field. We consider particles from nano-to-macro scale, including the manner of particle formation and implications for the fate of various elements that are important both for hydrothermal metal sulfide mineral formation and global ocean chemistry.

2. METHODS

2.1. Site description

Samples were collected from the hydrothermally active Niua South vent field (15.164°S, 173.757°W) during spring

2016 using the R/V *Falkor* and ROV *ROPOS* (FK160320). The vent field is situated within a 500-m diameter volcanic crater, at a depth of ~1160 mbsl on the southeast flank of Niuia South volcano, at the northern termination of the Tonga volcanic arc. It had previously been visited by the R/V *Roger Revelle* in 2012 (Resing et al., 2012) and Nautilus minerals (Jankowski, 2011). Boiling, focused, and diffuse flow samples were collected at different pressures and temperatures, and these have been described by Gartman et al. (2018). Most samples were collected in duplicate (Table 1).

2.2. Sampling

Fluid samples from Niuia were collected using titanium major samplers with the ROV *ROPOS*. Prior to sample collection, the temperature of the venting fluids were measured using the *ROPOS* high temperature probe. Between one and eight hours elapsed between sample collection and shipboard recovery of the ROV.

Samples were processed immediately upon shipboard recovery. Temperature and pH of the fluids was first recorded, with the temperature at surface always between 20 and 25 °C, compared to approximately 3.5 °C for *in-situ* bottom water at Niuia. Fluids were then subsampled for element analysis, including major elements and trace metals via ICP-MS, and sulfur via acid volatile sulfide/chromium reducible sulfur (AVS/CRS) analysis. Samples for trace metal analysis were frozen whole at sea, without filtration. Samples for AVS/CRS (both whole and 0.2 µm filtered) were fixed in 1 M NaOH and 0.1 M zinc acetate. Samplers were shaken continually during subsampling to maintain particle distribution in suspension. After subsampling was complete, particles in the remainder of the fluid were collected via centrifugation by the method of Gartman et al. (2014). The precipitate collected from centrifugation was capped with N₂ and frozen until analysis. The precipitate that resulted in tarnish on the sampler snorkel during sampling of the boiling vent was collected on parafilm, and frozen under nitrogen until analysis.

2.3. Fluid analyses

2.3.1. Inductively coupled plasma mass spectroscopy (ICP-MS)

For major elements, samples that had been acidified shipboard with HCl to below pH 1 were further leached upon return to shore with nitric acid for at least 48 h. Following secondary acidification, samples were filtered through a 0.2 µm Puradisc Nylon filter, diluted 100-fold in 2% HNO₃ and analyzed on a Perkin Elmer NexION 300Q ICP-MS. Beryllium 9, Ge 74 and Tl 205 were run as internal standards. Analytical precision determined by repeat analysis is better than 5%.

For trace metals, whole fluids (unfiltered) were acidified using subboiled HNO₃. Digestion of insoluble precipitates was performed over night at 160 °C in PFA vials (Saville) using a multistep mixed acid procedure with HF-aqua regia. Digested liquids were analyzed with both matrix-matched calibration and standard addition by high

resolution ICP-SF-MS (Thermo Scientific Element XR) in the ICP-MS Laboratory of the Institute of Geosciences, Kiel University, following the procedure of Garbe-Schönberg (1993) and Koschinsky et al. (2008). Analytical precision determined by repeat analyses of fluid samples is <1–7% RSD and limits of quantification (L.O.Q.) for each element are determined by repeat analysis of blanks on each instrument and monitored by control samples and duplicates. The accuracy of the results was assessed by analyzing NASS-5 Reference Seawater (NRCC National Research Council of Canada), IAPSO Standard Seawater (International Association for the Physical Sciences of the Ocean), NIST Standard Reference Material 1640a and 1643e (National Institute of Standards and Technology), and two in-house standards (JUB-1 and CAU Anna Louise black smoker hydrothermal fluids).

2.3.2. AVS/CRS distillations

Sulfur partitioning in the fluids was investigated using AVS/CRS. Samples were thawed and added to three-neck round-bottom flasks for distillation. Five mL of 5 M HCl were added through the septa to liberate AVS. After purging with nitrogen for 1.5 h, the liberated sulfide gas was trapped as ZnS in 10–15 mL of anoxic zinc acetate (5% w/v) in a glass test tube. To measure CRS, fresh zinc acetate was added to new test tubes, then 5 mL acidified Cr(II) (1.2 M) were injected into the reaction vessels. Cr (II) was prepared by reducing a Cr(III) solution with zinc metal under nitrogen flow. After the addition of Cr(II) the mixture was allowed to purge and trap H₂S for one hour. Sulfide in the traps was quantified using the methylene blue spectroscopic method (Cline, 1969). The detection limit for this method is 1 µM sulfide.

2.3.3. Multiple sulfur isotope analyses

Samples from AVS/CRS analysis preserved as ZnS were converted to Ag₂S upon addition of Ag₂NO₃ (1 M). The precipitate was allowed to age one week, then washed with 18.2 MΩ water (MilliQ) and diluted NH₄OH (1 M). Washed samples were dried overnight at 60 °C.

Silver sulfide was converted to SF₆ by reaction with excess F₂ at 300 °C for at least 10 h in Ni alloy reaction chambers. The SF₆ was then purified cryogenically and by preparative gas chromatography. Following purification, stable sulfur isotope abundances (³²S, ³³S, ³⁴S and ³⁶S) were measured with a Finnigan MAT 253 dual inlet mass spectrometer at m/z values of 127, 128 129 and 131 (³²SF₅⁺, ³³SF₅⁺, ³⁴SF₅⁺ and ³⁵SF₅⁺) (Ono et al., 2006). δ ³⁶S values have greater error due to the low natural abundance of ³⁶S and did not provide information additional to ³³S (McDermott et al., 2015). They are therefore not presented here.

2.3.3.1. Isotope notation. Isotopic composition is presented in per mil using standard δ notation relative to VCDT (Eq. (1))

$$\delta^{3x}\text{S} = \left(\frac{{}^{3x}\text{R}_{\text{sample}}}{{}^{3x}\text{R}_{\text{VCDT}}} - 1 \right) \times 1000 \quad (1)$$

in which ${}^{3x}\text{R} = {}^{3x}\text{S}/{}^{32}\text{S}$ ($x = 3$ or 4).

Minor isotope notation is presented using $\Delta^{33}\text{S}$ notation (Eq. (2)), which describes the mass-dependent deviation of $\delta^{33}\text{S}$ from a reference fractionation line (Farquhar et al., 2003). Precision for $\delta^{34}\text{S}$ is 0.5‰, and precision for $\Delta^{33}\text{S}$ is 0.02‰.

$$\Delta^{33}\text{S} = \delta^{33}\text{S} - 1000 \times \left[(\delta^{34}\text{S}/1000 + 1)^{0.515} - 1 \right] \quad (2)$$

2.4. (Nano)particle analyses

2.4.1. X-ray diffraction (XRD)

XRD was performed on samples that were centrifuged shipboard and stored under nitrogen and frozen until analysis. Upon return to shore, precipitates were evaporated onto a zero-diffraction Si wafer (MTI) for powder XRD. Approximately the same amount of material was used for each sample. Although samples underwent rinses with deionized water, some of the bulk XRD patterns contained halite peaks, which were excluded from semi-quantitative results as halite is assumed to be an evaporite from remnant seawater.

To analyze the snorkel tarnish, a circle was cut from the parafilm and placed directly on a zero-diffraction Si wafer. This scan was compared with a similarly prepared sample of ‘clean’ parafilm to remove diffraction peaks due to the parafilm.

Samples were run on an X’Pert3 powder diffractometer by Panalytical. Samples were scanned from 5 to 70° 2 θ using a Cu K α source. For each sample, the scan was performed three times, with a 0, –1, and +1 degree wobble and final scans were an average of all three scans, in order to account for preferential sample orientation that may have occurred due to evaporation. Search-match for phase identification and semi-quantitative analysis of diffractograms was performed using HighScore Plus by Panalytical. For a further check on similarity between scans, aside from phase ID and peak identification, HighScore plus was also used to compare scans using Principal Components Analysis (PCA) and Hierarchical Agglomerative Cluster Analysis of the profile data, after Hein et al. (2013). Only profile data were considered, and the Euclidean distance measure was used. Major minerals are approximately >25%, intermediate minerals are 5–25%, and minor minerals are <5% based on semi-quantitative analysis, however mineral quantification has high uncertainty given the low sample volumes analyzed.

2.4.2. Scanning electron microscopy/energy dispersive X-ray spectroscopy (SEM/EDS)

SEM/EDS was performed on samples that were centrifuged shipboard and stored under nitrogen and frozen until analysis. Pellets were re-suspended in 18.2 M Ω (Milli-Q®) purified water, then precipitated directly onto 12.5 mm Ted Pella aluminum stubs. Samples were then rinsed several times with Milli-Q® distilled water to remove salts and evaporated under nitrogen. Samples were analyzed using a Tescan VP-SEM in high vac mode. High-resolution imaging was performed at 3 kV, and elemental analyses were performed at 20 kV and 14 mm working

distance. Samples were run without conductive coating so that element analyses could be performed for all elements. Imaging was performed using both secondary electron and backscatter detectors, or a mix of the two detectors. Scale bars shown were added using ImageJ.

2.4.3. Transmission electron microscopy (TEM)

TEM was used to investigate particles falling below the resolution of SEM. TEM results for gold were obtained at Virginia Tech’s NanoEarth facility using a LaB₆ Jeol-2100 TEM, operated at 200 keV. Samples were embedded in SPUR resin and sectioned to a thickness of less than 100 nm.

TEM results for all other minerals was performed at Stanford Nano Shared Facilities (SNSF) using a Tecnai G2 F20 X-TWIN TEM at 200 keV. Samples were evaporated onto lacey carbon stubs using deionized water. EDS was performed using EDAX Genesis software and includes data collected from the entire field of view. Scale bars shown were added using ImageJ.

2.4.4. Micro Raman

Micro-Raman spectroscopy was performed specifically to obtain mineralogical information regarding bismuth telluride minerals identified via SEM/EDS. A Thermo Scientific DXR MicroRaman, a 532 nm laser and a high-resolution grating, with 1800 lines per mm were used. A 50 μm pinhole was usually used, resulting in an estimated spot size of 2.1 μm . OMNIC software was used to run and ID phases. Particles that had been previously identified using SEM were sought out. Spectra were collected in triplicates of between 30 and 60 s at 1 mW power using a 10 \times or 100 \times lens.

2.5. Solubility calculations

Solubility calculations were performed with PHREEQC version 3, using element concentrations obtained by ICP-MS and sulfur distillations. Magnesium is assumed to represent seawater entrainment into the hydrothermal fluids rather than an artifact of sampling. Sulfate was assumed to entrain linearly with magnesium, with zero Mg considered to correspond to pure hydrothermal fluid (Edmond et al., 1982). Calculations were performed at measured *in-situ* temperature and extrapolated *in-situ* pH. In addition to these considerations, it is assumed that particle formation during initial sampling is analogous to that occurring in the chimney.

3. RESULTS

3.1. Fluid chemistry

Element analyses for whole-fluids are presented in Table 1. Sodium and chlorine at Niua are higher than seawater, with the lowest values in the most dilute samples indicating that the effluent is a brine. Chloride/bromide ratios are similar to those in seawater, $1.57 \pm 0.13 \times 10^{-3}$. Iron is in excess to manganese and sulfur, and Fe/Mn ratios do not decrease as a function of Mg, indicating that

Table 1

Fluid concentrations of major elements and particle relevant elements for all samples at Niua. Results presented are whole fluid (unfiltered) concentrations.

Sample name	Dive number/ sampler	Description	T (°C)	Depth	Latitude	Longitude	pH	Mg (mM)	Si (mM)	Ca (mM)	K (mM)	Na (mM)	Cl (mM)
Boiling 1	1918 blue	Boiling	325	1164	−15.163162	−173.5747	3.14	4.0	15.3	22.9	59.8	550.2	645.9
Boiling 2	1918 yellow	Boiling	325	1163	−15.163162	−173.5747	3.84	15.0	11.4	20.3	48.8	534.3	627.5
Focused flow 1	1918 red	Focused Flow	302	1155	−15.162867	−173.57464	4.12	23.6	6.5	18.0	39.8	524.8	568.8
Focused flow 2	1918 orange	Focused Flow	302	1155	−15.162867	−173.57464	5.98	38.3	0.6	8.4	10.7	450.3	452.9
Focused flow 3	1919 yellow	Focused Flow	300	1151	−15.164768	−173.5736	3.36	3.4	14.6	21.2	48.0	521.3	622.8
Focused flow 4	1919 green	Focused Flow	300	1151	−15.164768	−173.5736	4.73	28.0	8.0	18.8	35.4	535.5	532.5
Focused flow 5	1919 gray	Focused Flow	316	1155	−15.164662	−173.57423	3.62	12.1	8.5	16.9	28.1	503.5	530.8
Focused flow 6	1919 red	Focused Flow	316	1155	−15.164662	−173.57423	4.43	22.8	7.6	16.0	40.1	524.8	601.0
Focused flow 7	1920 blue	Focused Flow	278	1146	−15.165502	−173.5739	4.57	21.1	6.0	10.5	18.7	462.8	597.9
Diffuse flow	1920 orange	Diffuse Flow	250	1142	−15.164893	−173.57293	4.14	31.4	6.2	16.2	32.3	525.0	594.1
Sample name	Br (mM)	Fe (μM)	Mn (μM)	Cu (μM)	Zn (μM)	Pb (μM)	Ag (nM)	Au (nM)	As (μM)	Bi (nM)	Te (nM)	Ba (μM)	Sr (μM)
Boiling 1	1.1	2980	1280	42.3	66.7	2.58	35.6	3.1	8.9	5.7	17.6	82.5	125
Boiling 2	1.0	2350	983	69.8	86.9	3.76	52.5	3.7	12.4	8.1	17.6	101	111
Focused flow 1	0.9	1600	725	37.4	54.8	2.32	37.1	2.9	8.6	8.4	11.2	61.1	108
Focused flow 2	0.7	161	54.4	30.9	26.4	1.51	19.8	3.0	2.8	9.1	10.4	43.3	96.7
Focused flow 3	0.9	3990	1390	50.9	100	4.52	61.0	1.6	14.3	7.2	16.8	109	152
Focused flow 4	0.7	1910	661	35.9	50.0	1.50	15.6	2.0	7.0	23.4	38.4	57.5	129
Focused flow 5	0.7	2460	982	55.6	70.7	2.58	40.7	3.1	9.8	6.0	13.6	57.7	123
Focused flow 6	1.0	1570	629	83.1	49.6	2.00	18.8	5.4	8.6	240	303	64.1	106
Focused flow 7	1.0	1360	591	13.0	43.3	1.41	18.6	1.6	6.1	0.6	3.2	37.5	110
Diffuse flow	1.0	1260	568	75.3	62.5	3.03	45.9	26.7	9.5	0.4	4.8	90.5	119

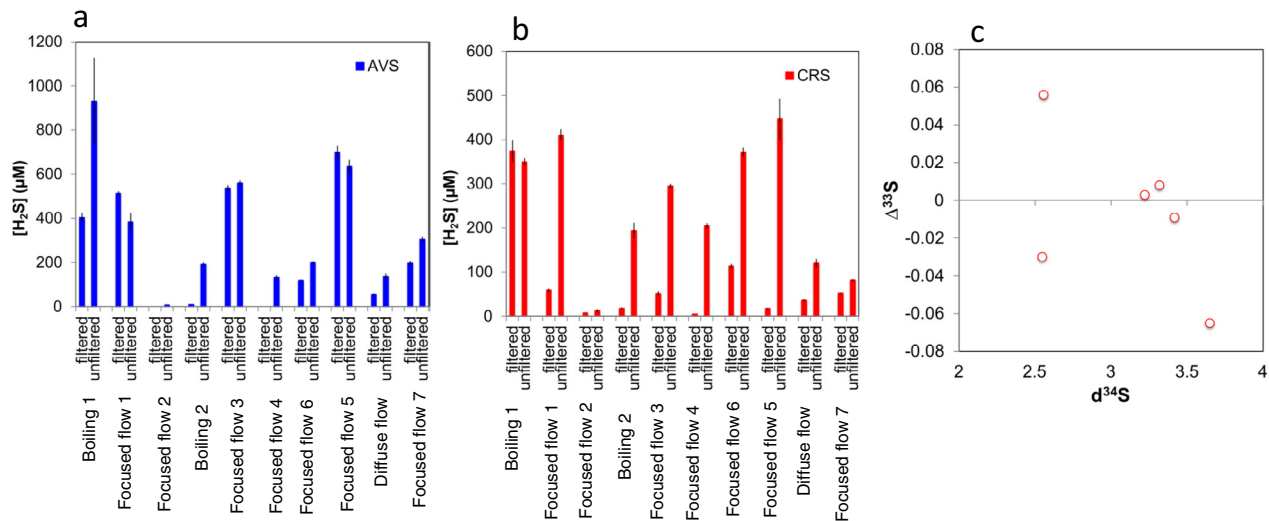


Fig. 1. AVS (a), CRS (b), and sulfur isotopes (c) from samples at Niua. The AVS/CRS ratios are highly variable, and samples at Niua are between 34 and 98% AVS. Isotope results were not obtained for all samples due to limited sample volume.

Table 2

Sulfur isotope results for fluids from Niua. All results are for total sulfide (AVS + CRS).

Sample	$\delta^{33}S$	$\delta^{34}S$	$\Delta^{33}S$
Boiling 1	1.75	3.42	−0.0090
Focused flow 1	1.28	2.55	−0.030
Focused flow 3	1.79	3.63	−0.065
Focused flow 5	1.66	3.22	0.0030
Focused flow 6	1.71	3.32	0.0080
Focused flow 7	1.37	2.56	0.056

precipitation of Fe containing minerals is not occurring rapidly upon seawater entrainment, consistent with $Fe \gg S$. AVS ranges up to 0.70 mM in the filtered fraction and 0.93 mM in the unfiltered fraction; CRS is a maximum of 0.37 mM in the filtered fraction, and 0.44 mM in the unfiltered fraction (Fig. 1). $\delta^{34}S$ ranges from 2.5 to 3.6, and $\Delta^{33}S$ ranges from −0.065 to 0.057. (Fig. 1, Table 2). Niua is not as acidic as some arc and back-arc fluids; the lowest pH measured shipboard was 3.14, in contrast to pH values below 2 measured at white and black smokers in Lau Basin, the southern Mariana Trough and the Okinawa trough (Gamo et al., 2006). A mixing curve of hydrothermal enrichments vs. Mg indicates that at Niua pure hydrothermal fluids trend toward zero Mg, (Table 1) validating the zero Mg endmember assumption used for seawater entrainment in solubility calculations.

3.2. Major mineralogy and microscopy

For all fluid samples collected at Niua, the dominant mineral identified by XRD was either barite, chalcopyrite, anhydrite, pyrite, or some combination of these. Sphalerite was also identified by XRD in four of the ten fluid samples (Fig. S3, Table 3). The majority of particles observable in the fluid samples via SEM can be represented in four broad classes. The first dominant particle type was tabular barite,

with average size varying between 1 and 5.5 μm in side length in different samples. Tabular barite visibly dominated both boiling and most of the focused flow samples, except for focused flow 2. Four samples, (boiling 2, focused flow 3, 5 and 7) consisted almost entirely of sub-micron and nanoscale particles and tabular barite (Figs. 2 and 3).

The second dominant particle class was aggregates of spherical particles containing varying ratios of Cu, Fe, Zn and S. These particles ranged from ~ 500 nm diameter with well-defined spherical morphology, to smaller sized particles with a diameter < 100 nm, with the size and morphology of smaller particles hard to distinguish consistently via SEM due to the size and aggregation (Fig. 3). TEM analysis confirmed the observation that Cu, Fe, Zn, As and S co-occur on small (< 50 nm) spatial scales in the same particle grouping, and that the individual particles may be as small as 2 nm (Fig. 4). In addition to occurring in mixed metal nanoparticles, arsenic was also observed to occur in discrete As-S or As-Pb-S. After tabular barite, these < 100 nm particles visibly dominated boiling samples and focused flow samples 3, 5 and 7 during SEM assessments. Based on XRD and TEM/ED results (Fig. 4) these particles were likely comprised of nanophase ZnS, with the other elements either adsorbed on the surface of or incorporated into the particles, based on XRD and TEM/ED results (Fig. 4). The submicron and nanophase ZnS gives both discrete diffraction points for sphalerite and diffuse diffraction rings (Fig. 4). The diffuse diffraction rings are similar to those attributed to synthetic nanophase ZnS (Fig. S5) that is neither an endmember to sphalerite or wurtzite (Vogel et al., 2000).

The third particle class consisted of larger ($> \sim 500$ nm), euhedral particles. These particles included FeS_2 (boiling sample 1, diffuse flow), PbS (focused flow 2, diffuse flow) and $CuFeS_2$ (diffuse flow). The most common morphology was spheroidal or framboidal ($FeS_2/CuFeS_2$) or octahedral (PbS), although cubic PbS and FeS_2 were also observed. The samples with cooler *in-situ* temperature, higher

Table 3

XRD results from black smoke precipitates. Results are only roughly quantitative as diffracted powder was of low and variable volume.

Sample name	Dive/bottle	Major	Intermediate	Minor
Boiling vent tarnish	1918 blue parafilm	Sulfur	Barite, pyrite, anhydrite, calcite	Chalcopyrite
Boiling 1	1918 blue	Barite, chalcopyrite	Pyrite	
Boiling 2	1918 yellow	Barite	Chalcopyrite, sphalerite	
Focused flow 1	1918 red	Barite, pyrite	Chalcopyrite	
Focused flow 2	1918 orange	Chalcopyrite, barite	Pyrite, sphalerite	
Focused flow 3	1919 yellow	Barite	Chalcopyrite, sphalerite	
Focused flow 4	1919 green	Anhydrite, chalcopyrite	Barite	
Focused flow 5	1919 gray	Barite	Anhydrite, pyrite, chalcopyrite	
Focused flow 6	1919 red	Anhydrite, chalcopyrite		Barite
Focused flow 7	1920 blue	Barite	Chalcopyrite, sphalerite	
Diffuse flow	1920 orange	Barite, chalcopyrite	Pyrite	

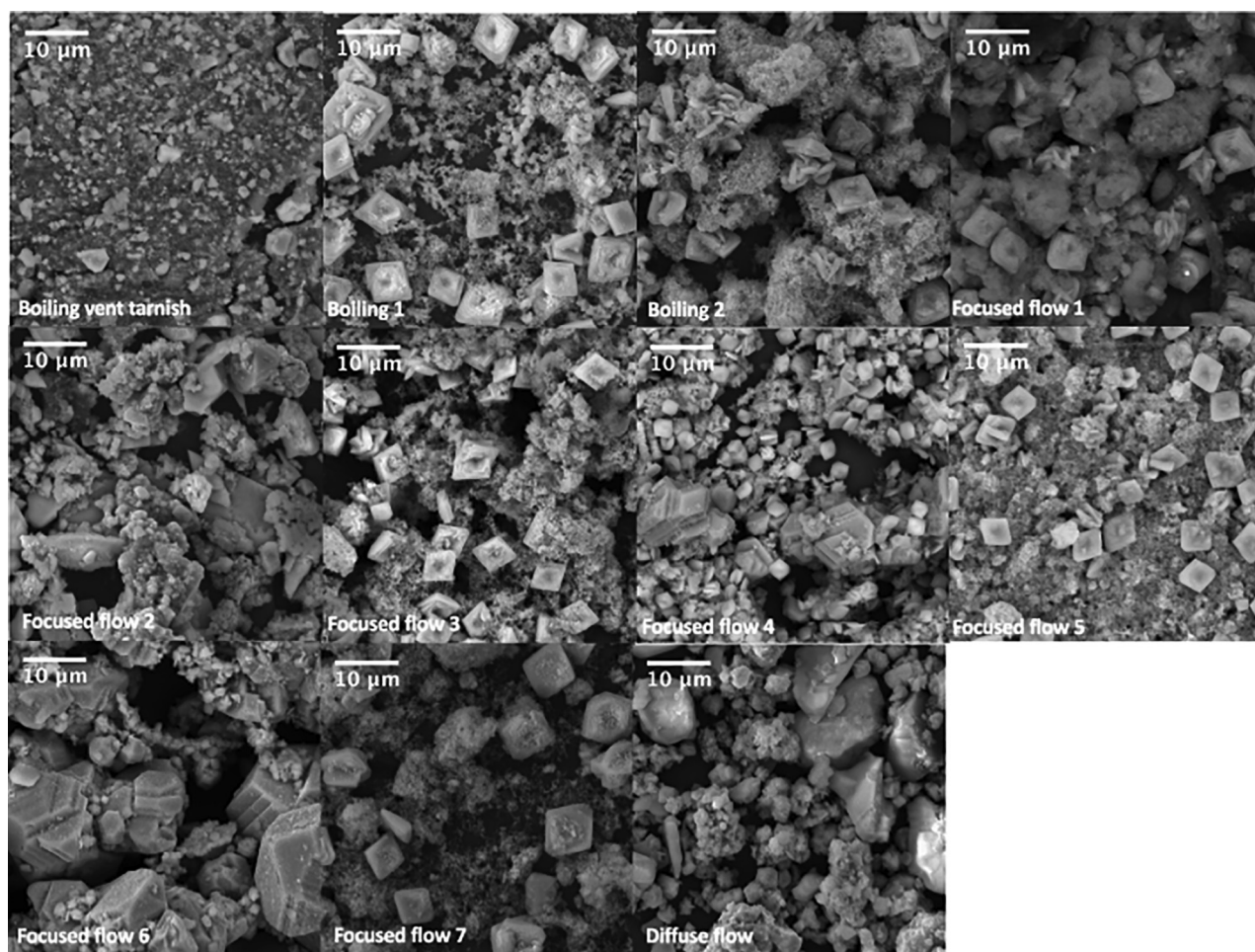


Fig. 2. Representative SEM images from all samples collected, images are all the same scale and descriptions of each sample are listed in Table 1.

shipboard pH and higher Mg concentrations contained a greater abundance of larger particles with well-defined morphology (Fig. 2). Some samples (boiling sample 2, focused flow sample 1, 3 and 7) contained no larger, euhedral particles aside from barite, and only contained barite and the small aggregates.

The last broad class of particles observed was entrained chimney fragments. These were often large and represent

the only >10 µm particles observed and exhibited broken edges (Fig S1). Six samples (boiling 2, focused flow 1, 2, 3, 4 and diffuse flow) contained some entrained chimney pieces. These were few and not representative of the sample, although they do contribute to bulk results, including total element concentrations and mineralogy (bulk XRD). Focused flow 6 contained the greatest number of entrained pieces determined both visually and by examining XRD

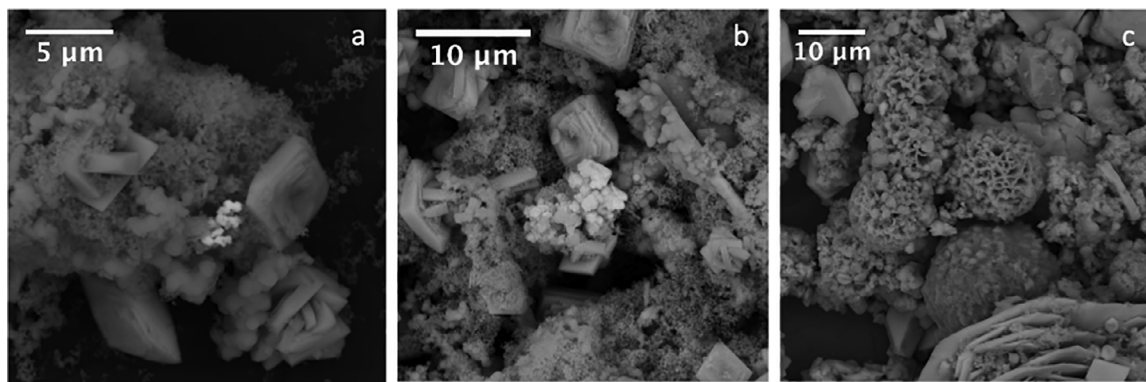


Fig. 3. Further details of variable particle morphologies represented in fluids from Niua and not represented in overview images presented in Fig. 2. a. From boiling vent 1; larger spheroids are ZnS; smaller particles are compositionally CuFeS₂ with variable As; bright spots contain Pb; tablets are barite. b. From boiling vent 1; discrete clumps are ZnS with As; bright center also contains Pb. c. Diffuse flow vent. Central spheres CuFeS₂; bottom sphere FeS₂.

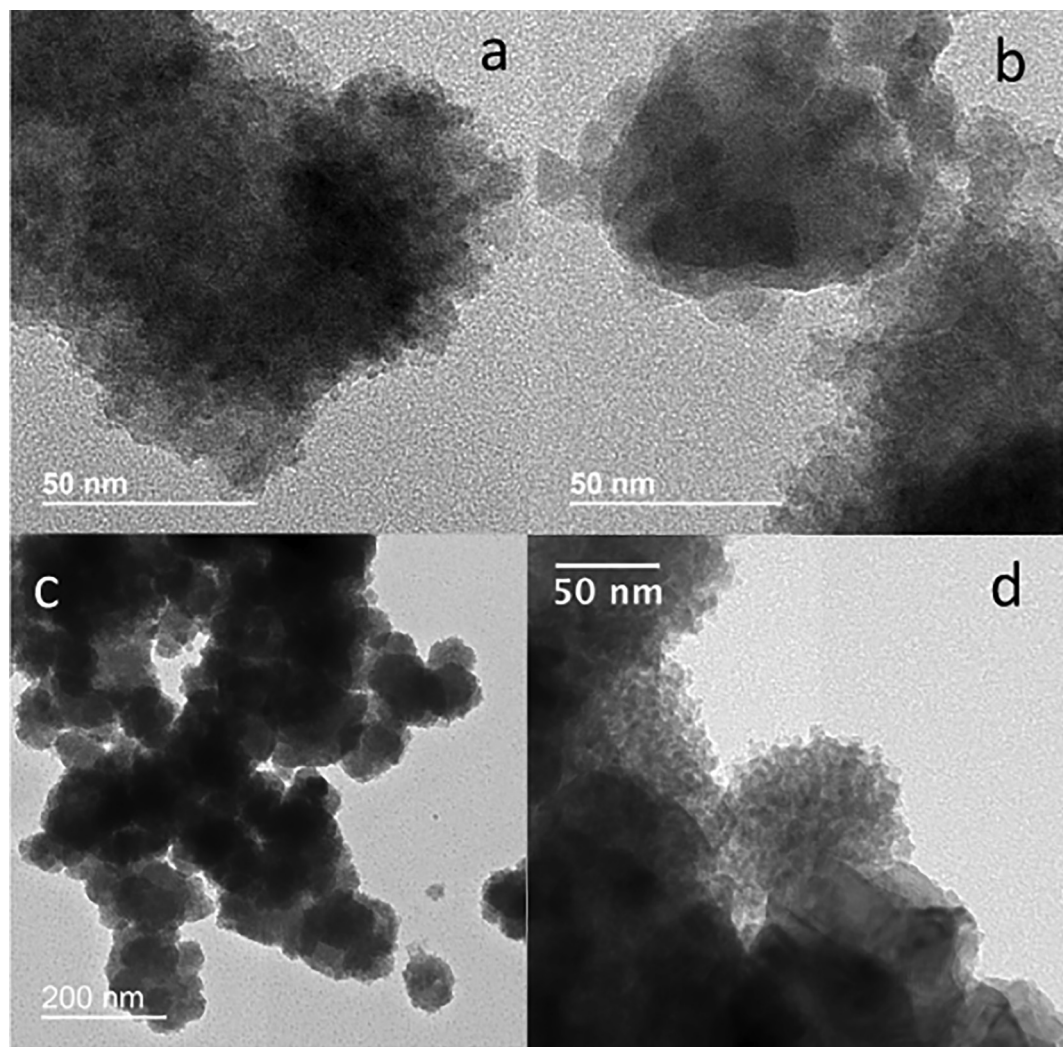


Fig. 4. TEM micrographs and electron diffraction for sample boiling 2 (a and b) focused flow 4 (c) and boiling 1 (d). Corresponding ED are shown in the appendix. The ED rings and spots can be explained by nano ZnS and sphalerite. In addition to Zn and S, Pb, As and Fe were detected via EDS.

results. Based on element ratios obtained by EDS, entrained chimney pieces are composed of either anhydrite, barite or chalcopyrite. This is consistent with the composition of the chimneys, which are dominated by chalcopyrite and minor pyrite lining the interiors of all chimneys, with anhydrite adjacent to chalcopyrite. (Fig. S2).

For the tarnish deposited on the sampler nozzle during boiling, SEM showed that the particles are a mix of a nanophase coating, as well as larger euhedral crystals. Tabular barite was not commonly observed by SEM on the snorkel tarnish; EDS showed the nanophase precipitates are largely composed of Fe, Cu and S. The tarnish collected from the boiling vent contained sulfur and calcite, in addition to barite, pyrite, anhydrite and chalcopyrite. The chalcopyrite exhibited peak broadening, indicating nanoscale minerals (Scherrer, 1918).

3.3. XRD clusters and solubility

Automated cluster analysis was performed on XRD diffractograms to provide further insight into bulk particle composition. Three groups were identified; one group (focused flow 4 and 6) contains some anhydrite; a second group (the tarnish on the nozzle and boiling 1) contained no entrained chimney pieces and exhibited broader peaks for most minerals; and all other samples formed one cluster (Fig. 5). The first three components explained approximately 80% of the variation between sample profiles; five components would be required to explain >90% of the variance. Peak intensity was not used as an input to the analysis, so the similarity is based on the presence or absence of minerals and not their relative abundances.

All major minerals (barite, chalcopyrite, galena, and pyrite) were supersaturated in all fluids at the point of collection, except for sphalerite, which was supersaturated in focused flow 1, 6, 7 and diffuse flow, and undersaturated in other samples (Fig. 6). Nanophase ZnS is abundant throughout the samples as evidenced by SEM/EDS,

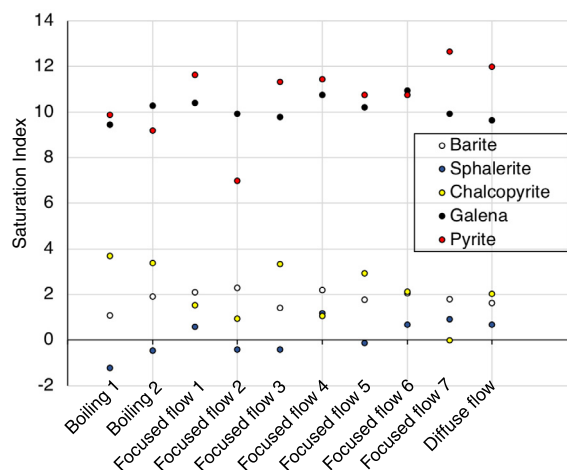


Fig. 6. Saturation index for major minerals at the conditions of collection measured by powder XRD calculated by PHREEQC.

TEM/ED and powder XRD, with powder XRD peaks apparent in samples focused flow 1 and 5; it is the only distinct “nanomineral” identifiable by powder XRD, defined as a nanoscale mineral that has no equivalent macromineral (Hochella et al., 2008).

3.4. Minor phases

Arsenic sulfides are inferred from EDS elemental ratios, however they are not identified mineralogically. SEM/EDS and TEM/ED/EDS results indicate that in addition to discrete As sulfides, As is likely also adsorbed to ZnS, and may be a major (10% atomic) constituent of both the larger (>100 μm) and smaller sulfide particles described above. The ZnS was in some cases crystalline sphalerite, and in some cases poorly crystalline nano ZnS.

Other particles identified via SEM include native Au (Gartman et al., 2018; Fig. 7) and bismuth tellurides

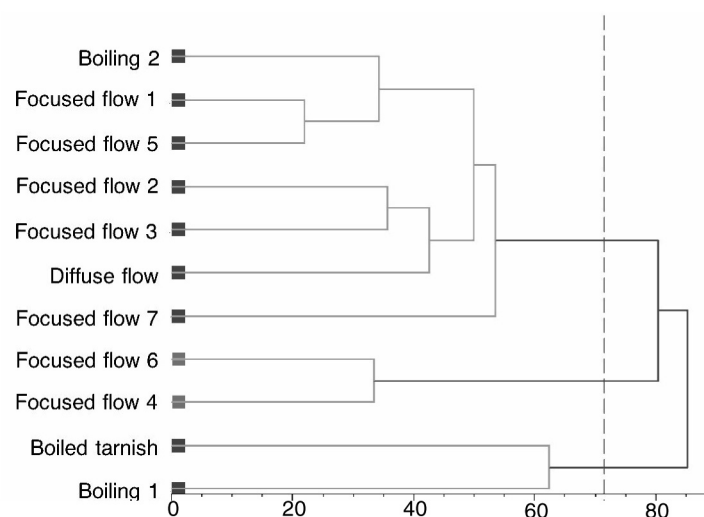


Fig. 5. Dendrogram representing an automated cluster analysis of diffractograms. Dashed line represents 70% dissimilarity and is used to break patterns into three groups.

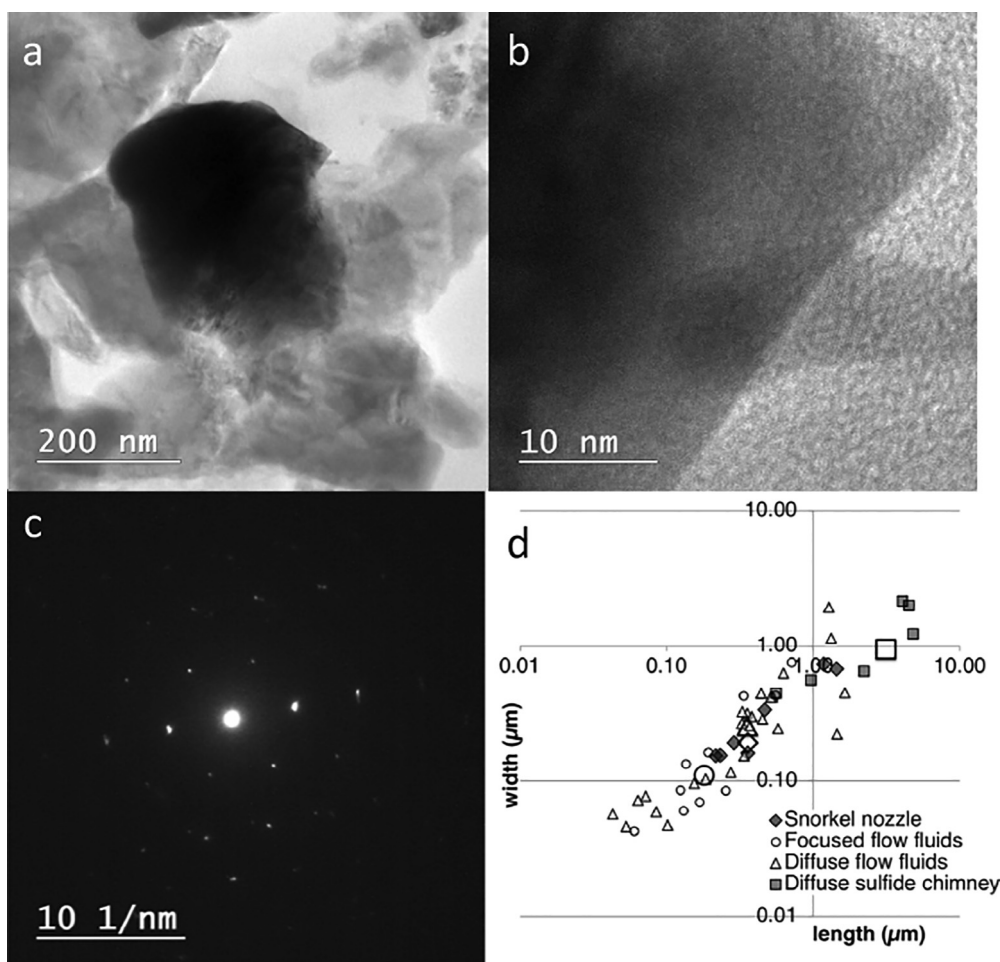


Fig. 7. TEM micrographs (a and b) and diffraction (c) of Au from the diffuse flow vent and (d) particle sizes from the particles measured via SEM.

(Fig. 8). Bismuth tellurides were mainly tabular and often hexagonal, and averaged $1 \times 0.6 \mu\text{m}$ ($\pm 0.4 \times 0.3 \mu\text{m}$) in tablet length and width and were typically $<200 \text{ nm}$ thick and often $<100 \text{ nm}$ in one dimension. Seventy-five Bi_xTe_y particles were found in focused flow 1, 3, 4, 5, and 6. These particles occur in samples containing the highest overall concentrations of both elements. The Bi/Te ratio in particles is considered uncertain due to the small particle size and variable sample topography during analyses. Raman spectroscopy demonstrated that tellurobismuthite accounts for at least some of the Bi_xTe_y particles identified (Fig. 8f), although most of the particles were too small to be identified under the 100x optical microscope lens.

4. DISCUSSION

4.1. Mineralogy of fluids

Fluids have long been known to transport minerals, with the detection of small (e.g., $<1 \mu\text{m}$) particles constrained by the techniques used. A compilation of minerals detected in hydrothermal plumes is presented in Table 4, and includes data collected at the East Pacific Rise $9^\circ 50' \text{N}$, several sites

on the Mid-Atlantic Ridge, and Juan de Fuca. Pyrite and chalcocopyrite occur in all locations, and sphalerite and pyrrhotite are also common. The major minerals found suspended in fluids at Niua include pyrite, sphalerite, chalcocopyrite, barite, and anhydrite, and are consistent with the dominant composition of the chimneys (Gartman et al., 2018) and solubility calculations (Fig. 6). As in other vent fields with temperatures below 350°C , samples taken at Niua are depleted in Cu relative to Fe due to chalcocopyrite precipitation (Metz and Trefry, 2000; Seyfried and Ding, 1993). Niua fluids have excess metals relative to sulfur, with $S_{\text{tot}}/(\text{Fe} + \text{Cu} + \text{Zn})$ ranging from 0.095 to 0.47. At Niua, AVS/CRS ratios are between 0.5 and 40 in the filtered phase and 0.6 and 4 in the whole fluid, indicating large variability in sulfur distribution between the two phases, and also that CRS (indicating recalcitrant sulfide minerals) is not clearly divided as a function of size. Fe/Cu ratios at Niua are similar to prior results in the Lau basin and are consistent with buffering by the hematite-magnetite assemblage (Seyfried and Ding, 1993).

Barite forms in hydrothermal fluids after the entrainment of seawater sulfate; at Niua, barite formation occurs at the point of boiling (i.e. on the snorkel tarnish) and later,

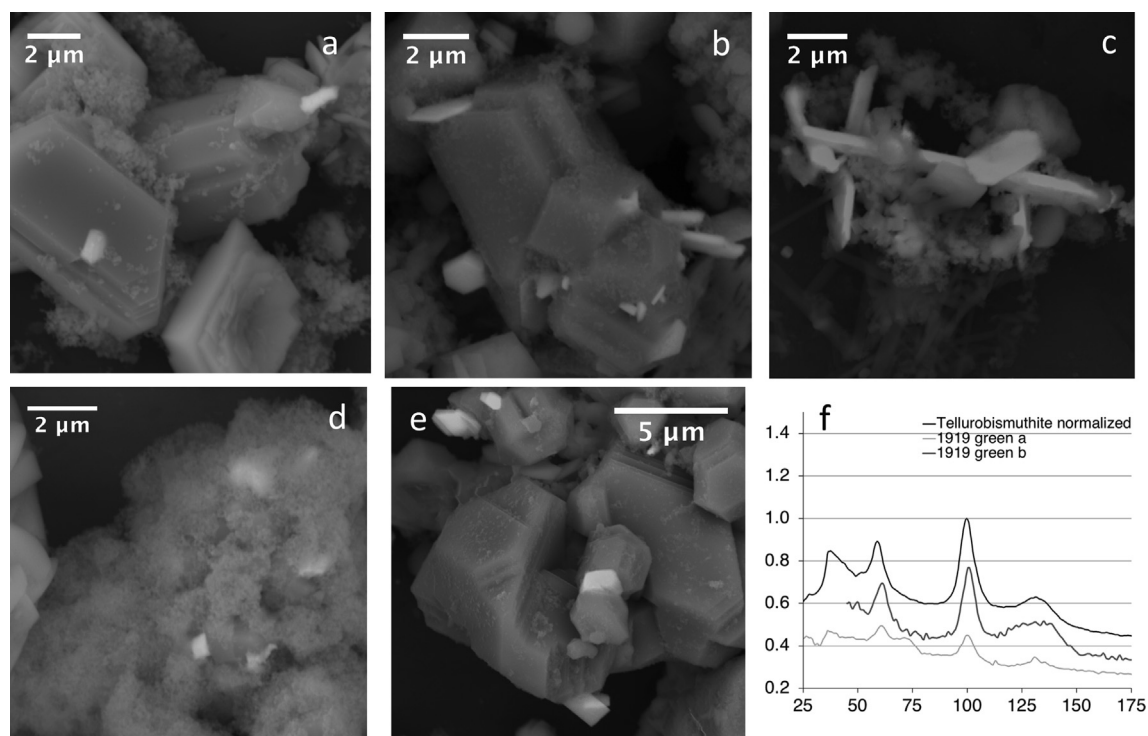


Fig. 8. SEM micrographs of bismuth tellurides from focused flow samples 1 (d), 3 (a) and 6 (b, c and e). Bright particles, often platelets, are the bismuth tellurides. Other euhedral particles are either barite (a) or chalcopryrite (a, b and e). In a and b some of the Bi_xTe_y particles are embedded in chalcopyrite. In sample d, they are embedded in the aggregate of nanoparticulate metal sulfides. Aggregates of smaller particles are some combination of Zn, Cu, Fe and S with variable ratios. f. Raman spectra bismuth telluride that is broadly consistent with the tellurobismuthite standard.

as the fluids continue to cool and mix. In contrast to the conductive cooling that occurs as fluids rise through the system, cooling and mixing during sampling are coupled. The fluid samples obtained at Niua exhibit between 6.5 and 72.6% seawater magnesium. This involves a minimum entrainment of ~ 1.9 mM sulfate, while the maximum barium measured was $109 \mu\text{M}$ and therefore always at least an order of magnitude lower than the sulfate. SEM examination revealed that for the majority of the samples, barite particles exhibited a narrow range of sizes ($1\text{--}5.5 \mu\text{m}$) although TEM results showed nanophase barite crystals (Fig. S4).

The majority of barite observed in fluids at Niua is tabular or a variation on tabular, with intergrown and twinned crystals common (Fig. 2, Fig. 9, Fig. S4). The side lengths of tabular barite particles were measured as another control on particle growth and showed a relationship with the Mg concentration of the fluids, and not barium concentration, shipboard pH, high temperature of the vent fluid, or time from sample collection to processing. Broadly, the side length of tabular barite decreased with increasing magnesium content (and corresponding sulfate entrainment). In addition, low Mg samples exhibited more regular barite morphologies, with tabular barite crystals dominating at low Mg, consistent with barite precipitation at higher temperature and lower degrees of supersaturation (Jamieson et al., 2016). Chains of smaller tablets appeared in focused flow 4 (53% seawater). The diffuse flow sample (60%

seawater) exhibited small, infrequent barite tabs, and no tabular barite was observed in focused flow 2 (73% seawater). The lack of observed barite in focused flow 2 is possibly related to the abundance of other minerals, which may have made the barite more difficult to observe, as focused flow 2 did exhibit barite peaks via XRD.

Sphalerite is variably saturated in the fluids at the point of collection (Fig. 6), and zinc sulfide nanoparticles are not observed via powder XRD in all samples although this may be related to variations in abundance of other minerals. The two samples most clearly exhibiting nano-ZnS via powder XRD did not include bulk sphalerite. Although discrete arsenic minerals were not detected via diffraction methods, the suggestion that large amounts of sorbed As are present on zinc sulfides is consistent with the tendency of arsenite to adsorb to metal sulfides (Bostick et al., 2003) and its association but uneven distribution relative to iron oxides and sulfides in previous studies (Breier et al., 2012). Breier et al., 2012 also found that As was positively correlated with both Fe and Zn in hydrothermal plume samples from EPR. Arsenic forms oxyanions in seawater and may have adsorbed onto the rising plume particles from seawater, however another possibility for the Zn-As correlation could be coupled Zn-As particles present at the point of discharge.

Bismuth tellurides, identified here, have not previously been identified in suspension in hydrothermal fluids, but bismuth tellurides including tellurobismuthite have been

Table 4

Compilation of minerals detected in hydrothermal plumes. References 2, 4, 5 and 6 include data from hot fluids; reference 1 includes data from up to 26 m above the vent, in the rising plume; and reference 3 includes data from the neutrally buoyant plume. References and locations: ¹Feely et al. (1990), ASHES vent field, Axial Volcano, Juan de Fuca Ridge; ²Klevenz et al. (2011), Logatchev I and 5°S, Mid-Atlantic Ridge; ³Breier et al. (2012), East Pacific Rise 9°50'N; ⁴Gartman et al. (2014), Rainbow, TAG and Snakepit, Mid-Atlantic Ridge; ⁵Findlay et al. (2014), Rainbow, TAG and Snakepit, Mid-Atlantic Ridge; ⁶Findlay et al. (2019), ⁷this study.

Mineral	Formula	Reference
Sulfides		
Pyrrhotite	Fe _(1-x) S _x	1,2,3
Mackinawite	FeS	3
Pyrite	FeS ₂	1,2,3,4,6,7
Marcasite	FeS ₂	1
Bornite	Cu ₅ FeS ₄	3
Cubanite	CuFe ₂ S ₃	3
Chalcopyrite	CuFeS ₂	1,2,3,4,6,7
Chalcocite	Cu ₂ S	3
Covellite	CuS	3
Digenite	Cu ₉ S ₅	3
Fukuchilite	Cu ₃ FeS ₈	3
Alabandite	MnS	3
Rambergite	MnS	3
Hauerite	MnS ₂	3
Sphalerite	ZnS	1,2,3,6,7
Wurtzite	ZnS	2
Nano-ZnS	ZnS	6,7
Oxides		
Ferrihydrite	Fe ₅ HO ₈ ·4H ₂ O	3
Maghemite	Fe ₂ O ₃	3
Magnetite	Fe ₃ O ₄	3
Crednerite	CuMnO ₂	3
Bixbyite	(Mn,Fe) ₂ O ₃	3
Franklinite	(Zn,Mn,Fe)(Fe,Mn) ₂ O ₄	3
Sulfates		
Anhydrite	CaSO ₄	1,2,6,7
Barite	BaSO ₄	1,2,6,7
Gordaite	Zn ₄ Na(OH) ₆ (SO ₄)Cl·6H ₂ O	6
Si-containing		
Amorphous Si	SiO ₂	1
Kaolinite	Al ₂ Si ₂ O ₅ (OH) ₄	4
Carbonates		
Calcite	CaCO ₃	4
Tellurides		
Tellurobismuthite	Bi ₂ Te ₃	7
Native elements		
Au	Au	7
S	S	2,3,4,5,6,7

identified in hydrothermal sulfide chimneys and are one of the major phases for bismuth, together with native Bi or Te (Monecke et al., 2016), which we do not observe here. The correlation between Te and Bi indicates that Bi_xTe_y particles are the dominant form of bismuth and tellurium in these fluids, although the Bi/Te ratio varies from 0.08 to 0.87 suggesting a number of different phases may be present.

4.2. Processes of precipitation

The location of particle nucleation and the extent or lack of growth is one of the primary controls on the emplacement of hydrothermally emitted elements, whether in hydrothermal chimneys, the metalliferous sediments that are most abundant near field, or dispersal farther into the ocean including transport for thousands of kilometers (Resing et al., 2015). At Niua, we identify several mechanisms of mineral precipitation, each with different implications for the fate of elements in the system: boiling, mixing, conductive cooling within the hydrothermal flow, and cooling related to mixing or as an artifact during recovery of the samplers (Fig. 10).

4.2.1. Boiling and subsurface particle precipitation

Phase separation in seafloor systems may occur over a range of temperatures and pressures, either near or far from the critical point. The effect of phase separation on fluid composition depends both on the temperature and pressure at which phase separation takes place, and on the composition of the fluid prior to phase separation (Monecke et al., 2014). The loss of volatiles upon boiling may result in ligand loss (e.g. sulfide) and affect the fluid pH (e.g. loss of CO₂); with physical changes that also occur (e.g. volume, temperature) considered to have less of an impact on metal transport (Drummond and Ohmoto, 1985). In addition to the liquid phase becoming more oxidizing due to loss of reducing volatiles such as H₂, and H₂S, experimental work has demonstrated that the entire system (resultant vapor and liquid) may become more oxidized post-phase separation, as the volume of the initial system increases and the reducing components are effectively diluted (Bischoff and Rosenbauer, 1984). At higher temperatures near the critical point, differences between the resultant separated phases are not as great (Foustoukos and Seyfried, 2007) but at shallower/lower temperature systems, such as Niua, metal deposition due to boiling may be more efficient (e.g. Monecke et al., 2014).

The snorkel tarnish collected from the boiling black smoker at Niua provides a snapshot of the minerals precipitated directly upon boiling. Although the cold snorkel could have induced further precipitation, the same tarnish was not observed in other vents. In other samples, the fluids have already boiled before venting and therefore precipitated some minerals and associated elements as a result of boiling. The direct precipitation of native gold as nanoparticles on the snorkel (Fig. 7; Gartman et al., 2018) as well as the abundance of other nanoparticles including nano-chalcopyrite (Fig. 5) is evidence of the rapid nucleation and quenching at the boiling fluid/seawater interface (Fig. 10). Further precipitation of elemental sulfur indicates evidence of redox cycling potentially in tandem with iron, further supported by the Δ³³S values. The abundance of both pyrite and sulfur on the snorkel tarnish indicate rapid oxidation at the boiling interface, more so than in samples where mixing is occurring without boiling and elemental sulfur is absent.

Precipitation in the high-temperature fluids below the seafloor (either due to boiling, cooling, or direct magmatic

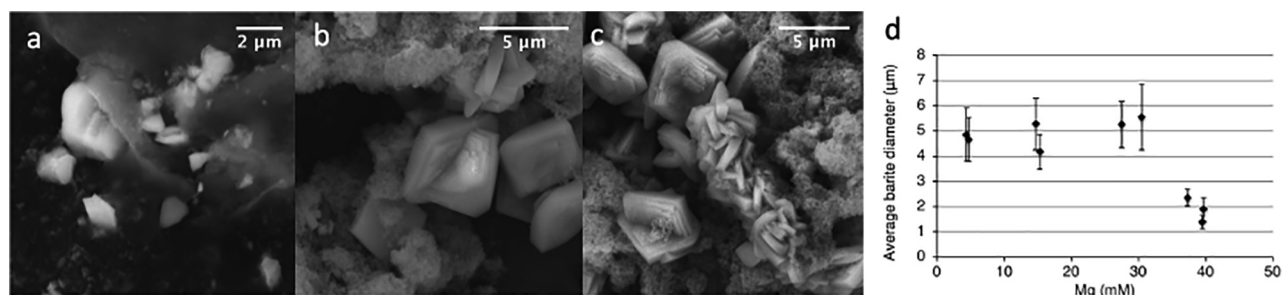


Fig. 9. Barite morphologies and particle size distribution of tabular barite particles at Niua. a is from the deposit on the snorkel tarnish; b and c are from focused flow 5. d plots the average diameter of tabular barite in all samples against the Mg concentration of the fluids.

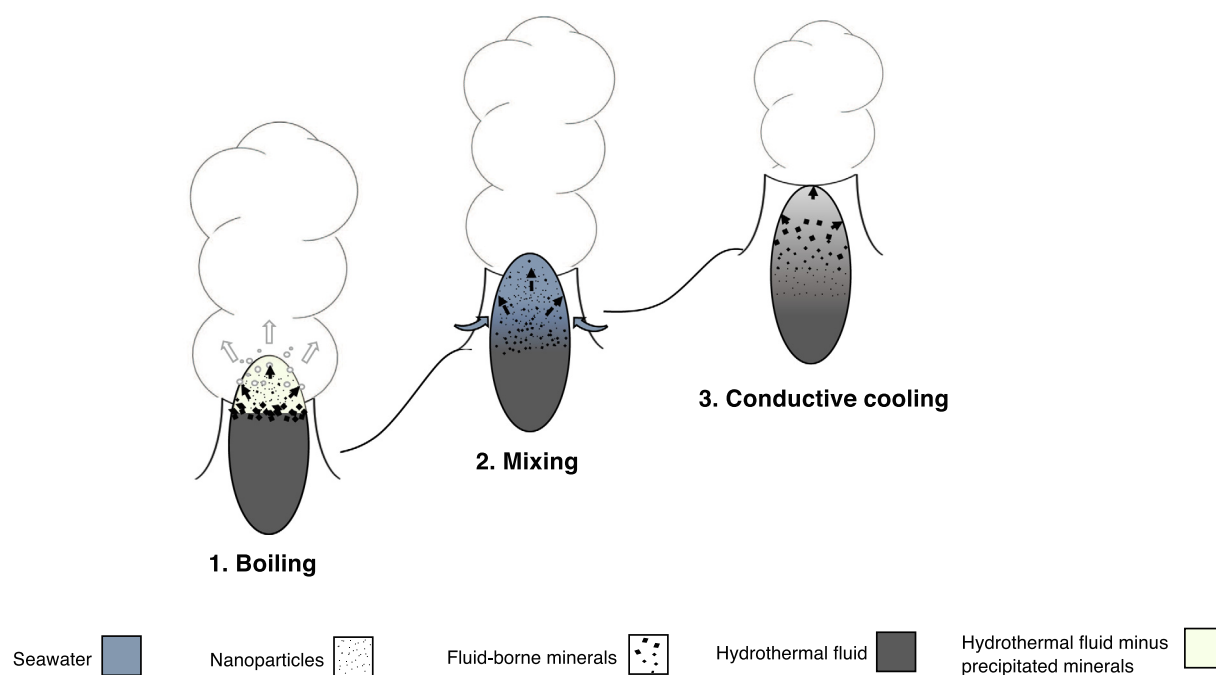


Fig. 10. Processes of precipitation occurring at Niua. 1. Boiling results in rapid vapor exsolution leading to sulfide (ligand) loss and deposition. Redox changes occur due to H_2 and H_2S loss as well as volume expansion. The precipitation zone is at the boiling horizon. Rapid particle nucleation occurs, as well as scaling when boiling is within a restricted zone. Scaling will result in particle deposition, whereas nanoparticles may undergo transport. 2. Mixing with seawater causes reagent concentrations to abruptly shift as two reservoirs mix together at meter-per-second rates, encouraging nucleation while limiting growth. Precipitation may be induced by the addition of reagents (e.g. SO_4^{2-}). Rapid dilution of hydrothermal fluid related to fluid flow rate may lead to abundant nucleation and little time for growth encouraging nanoparticle formation in a non-steady state process. The precipitation zone is at the interface between the reservoirs. Particle aggregation will limit transport. 3. Conductive cooling occurs in a fixed reservoir of reactants and no dilution means particle growth is encouraged until limiting reagents are consumed; reagent concentrations drawdown slowly as a result of precipitation, with an otherwise stable reservoir. Particle growth is encouraged. The precipitation zone is within the reservoir as the fluids cool, and particle growth may limit transport. Cooling during sampler recovery is analogous to process 3, conductive cooling as it occurs in a fixed reservoir of reactants. The rate of cooling is artificially slowed by the sampler, and particle growth is encouraged until limiting reagents are consumed, encouraging the formation of larger particles. Processes 1–3 often co-occur, complicating assessments. For instance, fluids may have boiled in the subsurface prior to undergoing conductive cooling during rise and mixing with seawater upon emission, as occurs at Niua. At Niua, the vertical distance from the deepest vent, which is the vent observed to be boiling, and the shallowest, diffuse flow vent, is approximately 20 m.

input) is indicated by elements that show no clear relationship to Mg. For example, Bi and Te do not show dilution with increasing Mg, as other elements do (Supplementary Table 1). The fact that many of the Bi-Te particles are embedded in chalcopyrite grains (Fig. 8) indicates that the precipitation of Bi-tellurides occurred prior to the euhedral chalcopyrite. Ciobanu et al. (2006) suggests that Bi-Te rich

melts form when a system experiences abrupt changes in redox state. The $\Delta^{33}S$ data of these fluids support the possibility of abrupt redox cycling (Kamyshny et al., 2014), but do not provide evidence for magmatic input. SO_2 is unstable below 350 °C so any gas phase loss would have occurred prior to the seafloor boiling observed at Niua; below 350 °C, SO_2 hydration and disproportionation results

dominantly in sulfite and sulfate species (Butterfield et al., 2011) that would not be trapped during AVS/CRS fixation, as well as sulfide and sulfur, which would be. Although gold and bismuth minerals are often found together in ore systems and it has been suggested that liquid bismuth may serve to aggregate gold (e.g. Törmänen and Koski, 2006; Tooth et al., 2011) no gold-bismuth minerals (e.g. maldonite) nor elemental bismuth or tellurium were observed, and gold and bismuth show different patterns of enrichment in the fluids (Table S1) and corresponding chimneys (Peterkin et al., 2018). The lack of co-enrichment of Bi, Te and Au is further evidence that the bismuth tellurides precipitated from solution rather than melt, as the presence of liquid Bi in the melt should have resulted in co-enrichment of Au (Tooth et al., 2011). Instead, all Bi is present as Bi_xTe_y particles which occur as ‘free’ particles in the system as well as mineral inclusions, and the bismuth telluride morphology is similar to particles synthesized from solution (e.g. Zhang et al., 2008).

4.2.2. Particle precipitation during cooling and mixing

Mixing and cooling often co-occur, but can have separate effects on mineral precipitation. Rapid mixing and resultant rapid fluid dilution will result in abundant particle nucleation and little time for growth, whereas conductive cooling with little mixing will result in larger minerals, as there is longer exposure time to growth conditions (Fig. 10). Klevenz et al. (2011) found via reaction path modeling that greater precipitation occurs with mixing than by conductive cooling alone, although the effect varied between minerals. At Niua, the precipitation of zinc sulfide nanoparticles in many of the samples is consistent with rapid nucleation and limited growth, and is suggested to occur rapidly upon hydrothermal fluid/seawater mixing. In contrast, the coarsely crystalline sphalerite and other metal sulfides precipitate upon mixing and/or cooling, as particle size and crystallinity increases for cooler fluids with higher Mg content. Sphalerite is saturated in the focused flow 1, 3, 5, 7, and in the diffuse flow under the conditions at which the fluids were collected as expected, since the saturation index of sphalerite increases for all samples as the fluids cool.

Sulfur isotope analyses are relevant for understanding endmember fluid composition, and post-emission element cycling. The $\delta^{34}\text{S}$ results from fluids at Niua range from 2.5 to 3.6‰ and are consistent with minor seawater entrainment or isotope exchange between sulfate and sulfide, as mantle sulfur has a $\delta^{34}\text{S}$ value of about zero ‰ (Ono et al., 2007). There is no evidence of disproportionation of SO_2 , which would be indicated by negative $\delta^{34}\text{S}$ values for sulfide. $\Delta^{33}\text{S}$ values from samples at Niua predominantly reflect reduction of seawater sulfate, with either very minor or no impact from isotope exchange with anhydrite (Ono et al., 2007). Notable exceptions are focused flow 7, which is consistent with full isotope equilibration between sulfide and anhydrite, and focused flow 3, whose strongly negative $\Delta^{33}\text{S}$ may reflect abiotic cycling of sulfur (e.g. Kamyshny et al., 2014). The large spread in $\Delta^{33}\text{S}$ indicates that S may be affected by different flow-path dependent processes during fluid mixing, such as redox cycling, isotope

exchange and particle formation, even though the fluid originates from a single source.

4.2.3. Possible artifacts of sampling

Two major potential artifact sets exist in this sample set; the possibility of particle formation in the sampler during recovery, and the entrainment of particles that were broken off from the hydrothermal chimney during sampling. Each possibility needs to be examined on a sample by sample (entrainment) and mineral specific (formation) basis. In the case of the abundant tabular barite, its morphology and experimentally determined kinetics of precipitation suggest that it is formed during sampling. Although barite was supersaturated in all samples under conditions relevant to the point of collection (Fig. 6) and barite precipitation kinetics are rapid, barite would continue to grow for minutes under these conditions (Gardner and Nancollas, 1983; Zhen-Wu et al., 2016), during which the fluids cooled. As a result, although barite is saturated *in situ* (Fig. 6) and is also a major component of the chimneys, the barite we observe in the sampled black smoke is likely of limited relevance to *in situ* hydrothermal plume mineral formation. This is supported by the observed correlation of barite crystal size and the Mg content of the sampled fluids. The decrease in particle size and the increased irregularity of the barite particles as a result of seawater entrainment could be related to a shift from growth control to nucleation control as the supersaturation increased with increasing seawater (SO_4) content, the rate of nucleation would likewise increase (Steefel and Van Cappellen, 1990; Jamieson et al., 2016). Mineral size, including for barite, does not correlate with time of sampler recovery (between 1 and 8 h, Section 2.2). Coupled with the rapid timescale of mineral precipitation kinetics noted above, the time between sampling and recovery does not result in systematic artifacts in this sample set.

A major challenge in characterizing particles in hydrothermal fluids is the point of filtration. Studies that have operationally defined nanoparticles based on the chemical reactivity of fluids (e.g. sequential acid leaching and sulfur reduction) that pass a filter note that the measured concentrations likely reflect underestimates due to aggregation of nanoparticles during filtration (Yücel et al., 2011; Gartman et al., 2014; Findlay et al., 2015). Studies attempting to compare *in situ* and *ex situ* filtration (Cotte et al., 2015) further note that *ex situ* filtration underestimates the “dissolved” fraction; however *in situ* filtration is only feasible to perform on lower temperature fluids. This difficulty has previously been noted for high temperature studies performing *ex situ* filtration (e.g. Schmidt et al., 2007; Hannington and Garbe-Schöenberg, 2019).

4.3. (Nano)particle fate

4.3.1. Local transport and emplacement

The role of nanoparticles in the fate of elements in hydrothermal systems will depend on the behavior of these particles within hydrothermal fluids and across the hydrothermal fluid-seawater boundary. Nanoparticles are defined as those with one or more dimension <100 nm,

due to the fact that within the nanoscale range, mineral properties may begin to deviate from those of a bulk mineral; these deviations are most important toward the smaller end of this range (Hochella et al., 2008). Colloids encompass nanoparticles and as well as slightly larger particles, and are defined as sub-micron particles, with the term meaningful because their size indicates that Brownian motion may be more important than gravitational settling, indicating the possibility of suspension and transport (Russel et al., 1989). Therefore, suspensions of submicron (colloids) and nanoscale minerals raise the possibility of increased element transport because they exhibit different chemical stability than dissolved species, with nanoparticles also differing in behavior from larger particles with the same mineralogy (Hochella et al., 2008). Additionally, nanoparticles may affect the sedimentation of other particles co-occurring in solution through charge buildup (Tohver et al., 2001). The stability of suspended submicron particles (colloidal suspensions) through time depends on several factors including surface charge and sterics (as influenced by surface functional groups), pH, and ionic strength. The solution temperature also affects stability by influencing the rate of particle collisions (Russel et al., 1989). The behavior of suspended particles is complicated in natural systems such as Niua by the inhomogeneity of the solution, wherein the dispersion is suspended in a heterogeneous fluid that contains temperature and ionic strength gradients as well as other particles. Processes of fluid flow and abundant low molecular weight organics, and with larger organics entrained along with seawater (Hawkes et al., 2015) also provides additional means by which the particles remain suspended in solution until destabilized by variation in fluid conditions (Sharma et al., 2009), in this case cooling. At Niua, as for most natural systems, the surface functional groups of the particles, the resulting surface charge, and subsequent repulsion between particles are not known. Gold appears to undergo transport as colloidal particles within the Niua system during fluid rise and conductive cooling, prior to fluid emission into seawater (Gartman et al., 2018); based on the density of these particles and their growth in the high temperature fluids, they are unlikely to undergo significant transport after emission into seawater.

Although other minerals appear to be abundant as nanoparticles and colloids (e.g. ZnS, chalcopyrite, bismuth tellurides), we do not see evidence that minerals other than Au were transported within the hydrothermal system in a way that resulted in element transport patterns distinctly different from those that could occur with larger ($>1\ \mu\text{m}$) particles or truly dissolved phases. There are several possible reasons for this. First, if an element is incorporated into several minerals or different sizes of the same mineral, or if nanoparticles and dissolved species of the same element occur concomitantly, there will not be a distinctive trend in the bulk element transport and it will be necessary to trace specific phases rather than elements (e.g. nanoparticulate pyrite rather than Fe, Yücel et al., 2011). Also, if nanoparticles are associated with larger mineral phases, either through incorporation (as we observe with bismuth tellurides) or through aggregation or adsorption, they will be subject to more rapid settling than discrete

nanoparticles, and their behavior in the bulk fluid will be like that of larger particles. Zinc sulfide nanoparticles are abundant in the samples and appear to remain nano-scale even as aggregates, however our dataset gives no indication as to whether zinc sulfide nanoparticles undergo transport away from the vent zone, although nanophase ZnS has previously been observed in the diffuse flow zone of hydrothermal vents via *in situ* electrochemical methods (Hsu-Kim et al., 2008). A potential consequence of the precipitation of nano- ZnS may be the suppression of bulk sphalerite or wurtzite formation. ZnS nanoparticles have been reported to undergo two phase coarsening (Huang et al., 2003) that is quite slow, and even at 225 °C, particles remained in the nanoscale size range after 100 h. Other studies have found that colloidal ZnS and sphalerite do not equilibrate, even over several months at room temperature (Daskalakis and Helz, 1993), meaning that once formed in hydrothermal environments like Niua, nano- ZnS may resist growth and remain nano-scale. As a result, physical transport and aggregation processes will dictate metal accumulation; the powder diffraction pattern and electron microscope imaging of the ZnS nanoparticles described here from Niua are quite similar to those described at Lake Kivu in 1972, which resulted in significant accumulation of zinc in the water column in resinous globules (Degens et al., 1972).

Although the potential for transport is the most frequently discussed reason to consider nanoparticle emission in hydrothermal fluids, local behavior of nanoparticles may be important for other processes occurring in hydrothermal systems. Previous studies have suggested nano-inclusions of conducting phases as potential reasons that semi-conductor sulfides exhibit metal like conductivity (Nakamura et al., 2010), as well as a possible reason that natural chalcopyrite has been observed to exhibit thermoelectric properties (Ang et al., 2015). Two of the minor mineral phases that occur with frequency in fluids at Niua have thermoelectric (BiTe) and photoelectric (nano Au) properties; both of which could contribute to conduction and electricity generation at chimneys. Heat is integral to hydrothermal systems and light may be generated in certain systems by several processes, including thermal radiation. Light may be particularly important in boiling systems as chemiluminescence, crystalloluminescence, and vapor bubble luminescence are other suggested mechanisms for light generation (Reynolds and Lutz, 2001; White et al., 2002). Even assuming a negligible photoelectric contribution from nano Au, inclusion of gold nanoparticles in bulk semiconductors will increase conductivity. All of these potential effects of nanoparticles are physico-chemically relevant for microbial interactions with chimneys, especially including extracellular electron transfer. However, the thermal stability of nanoparticles in hydrothermal chimneys is largely unknown, and for most minerals the longevity of nanoparticles when maintained at elevated temperatures, remains to be determined (e.g. Reich et al., 2006).

4.3.2. Potential for global transport

First principles (Hochella et al., 2012) and data-based (Gartman et al., 2014) estimates of hydrothermal

iron-sulfide nanoparticles emissions have been made and are in broad agreement; however, as demonstrated here, hydrothermal vents emit a wide variety of minerals to the global ocean which lack simple methods of quantification, and a full understanding of the emissions of particles, nanoparticles and colloids and their impact on global process and fluxes beyond the immediate vent zone requires further work. As observed at Niua (Figs. 4 and 9) nanoparticles may occur as metastable species, depositing in the chimneys and either growing or becoming incorporated into larger particles. If they remain in suspension as discrete particles, they may rise with the buoyant plume, possibly aggregating with either organic material or other minerals. Breier et al. (2012) observed abundant nanoparticle aggregation in the rising plume at EPR 9°N. Integrated studies considering particle transport from the vent zone to far field plume in the same system do not exist, and processes will vary among sites given particulars of hydrothermal geochemistry, temperature, fluid emission and local oceanographic conditions. Among other factors, the bulk geochemistry, including metal/sulfide ratios in fluid, will be important for the transport of metals as metal sulfide nanoparticles relative to metal-organic complexes. The magnitude of these processes is difficult to determine, but isotopic evidence may suggest the relative importance of each process farther afield (Rouxel et al., 2016). Fluid flow rates are likely a first order control on bulk vs nanoparticle metal sulfide precipitation, as greater flow rates would promote nucleation while minimizing growth, consistent with our observations here (Fig. 10). If precipitation does not occur until the interface with seawater is reached, the formation of nanoparticles will likely dominate metal mass balance, as suggested for the nano-ZnS at Niua. There is evidence that certain mineral nanoparticles behave conservatively, at least within the first meter of mixing (Findlay et al., 2015, 2019); however, the extent of transport beyond that point is unclear. As seawater mixing and cooling are major controls on particle precipitation, the entrainment of seawater into porous chimneys and variability therein (Tivey et al., 2002) should influence the timing of mineral precipitation and will be less variable in high temperature chimneys that do not exhibit tidal variability. Oceanic transport can occur even for larger particles resulting from organic entrainment due to their low density (Fitzsimmons et al., 2017) although these particles are likely dynamic and change through time, and do not represent discrete, single crystal minerals. Additionally, the presence of microbially produced organic matter may affect not only mineral transport far field, but also mineral-mineral attachment in chimneys (Gartman et al., 2017) and in sulfide-poor systems will provide primary complexation and influence mineralogy of metals that escape immediate inorganic precipitation (Toner et al., 2012).

5. CONCLUSIONS

The particle geochemistry of hydrothermal black smoke at Niua vent field has been examined in order to connect nano-to macro-scale mineralizing processes and to consider the location of precipitation in order to link growth of local

hydrothermal deposits, hydrothermal sediments, and the transport of hydrothermal elements away from the vent zone. Iron, copper and zinc sulfides, and calcium and barium sulfates are the most prevalent particles in the fluids at Niua, as has been shown for other vents in prior work. Different modes of particle formation, transport and growth are suggested for these (nano)particles, including precipitation as colloids upon boiling (gold), precipitation and growth upon mixing, at times as an artifact complicating *ex-situ* determination (barite), and potentially sub-seafloor formation via conductive cooling (bismuth tellurides). Although the hydrothermal vent-seawater interface provides potentially ‘ideal’ natural location for nanoparticle formation, with rapid particle nucleation and conditions limiting particle growth, these conditions are mainly realized under conditions with rapid rates of mixing and low rates of conductive cooling. Further, quantifying the abundance of these nanoparticles and distinguishing transport-relevant processes from mere presence as nanoparticles remains a challenge for the diversity of nanoparticles that occur, as they may be entrained in other minerals by the time they are emitted (e.g. bismuth tellurides) or occur across a range of sizes, crystallinity and aggregation states (zinc sulfides). We demonstrate that the point of precipitation and the potential fates differ for each specific mineral, and that long-distance mineral transport is not the only possible or consequential fate for nanoparticles emitted from hydrothermal vents.

Declaration of Competing Interest

None.

ACKNOWLEDGEMENTS

We would like to thank the Schmidt Ocean Institute for providing ship time, as well as the crew of the R/V Falkor and the ROV ROPOS for their skilled support. We thank the Kingdom of Tonga for permitting this work within their territorial waters. This work used shared facilities at the Virginia Tech National Center for Earth and Environmental Nanotechnology Infrastructure (NanoEarth), a member of the National Nanotechnology Coordinated Infrastructure (NNCI), supported by NSF (ECCS 1542100) and we thank Debora Berti at the NanoEarth facility for performing some of the TEM analysis. We thank Andrea Foster for use of the microRaman and Christopher Conaway for the IC analyses. TK acknowledges support of general cruise logistics through the Helmholtz Alliance ROBEX. Financial support for this work was provided by GEOMAR – Helmholtz Centre for Ocean Research Kiel and an NSERC Discovery grant to MH and from DFG Major Instrumentation grant to DGS at Kiel University. AF acknowledges funding from a Fulbright Postdoctoral Fellowship and from a Marie Curie European Fellowship (SedSulphOx, MSCA746872). JWJ acknowledges funding from the Canada Research Chair Program and a Newfoundland RDC Ignite grant. A subsidy for mobilization of ROPOS provided by CSSF was enabled by the Canada Foundation for Innovation Major Science Initiatives Fund (CFI MSI). All data are included in tables in the manuscript. Further data, including raw SEM/ TEM image files are available upon request. Any use of trade, firm, or product names is for descriptive purposes only and does not imply endorsement by the U.S. Government.

APPENDIX A. SUPPLEMENTARY MATERIAL

Supplementary data to this article can be found online at <https://doi.org/10.1016/j.gca.2019.06.045>.

REFERENCES

- Ang R., Khan A. U., Tsujii N., Takai K., Nakamura R. and Mori T. (2015) Thermoelectricity generation and electron-agnon scattering in a natural chalcopyrite mineral from a deep-sea hydrothermal vent. *Angew. Chem.* **54**, 1–6.
- Bischoff J. L. and Rosenbauer R. J. (1984) The critical point and two-phase boundary of seawater, 200–500°C. *Earth. Planet. Sci. Lett.* **68**, 172–180.
- Bostick B. C., Fendorf S. and Manning B. A. (2003) Arsenite adsorption on galena (PbS) and sphalerite (ZnS). *Geochim. Cosmochim. Acta.* **67**(5), 895–907.
- Breier J. A., Toner B. M., Fakra S. C., Marcus M. A., White S. N., Thurnherr A. M. and German C. R. (2012) Sulfur, sulfides, oxides and organic matter aggregated in submarine hydrothermal plumes at 9°50'N East Pacific Rise. *Geochim. Cosmochim. Acta.* **88**, 216–236.
- Butterfield D. A., Nakamura K., Takano B., Lilley M. D., Lupton J. E., Resing J. A. and Roe K. K. (2011) High SO₂ flux, sulfur accumulation, and gas fractionation at an erupting submarine volcano. *Geology* **39**, 803–806.
- Ciobanu C. L., Cook N. J. and Spry P. G. (2006) Telluride and selenide minerals in gold deposits- how and why? *Mineral. Petrol.* **87**, 163–169.
- Cline J. D. (1969) Spectrophotometric determination of hydrogen sulfide in natural waters. *Limnol. Oceanogr.* **14**, 454–458.
- Cotte L., Waeles M., Pernet-Coudrier B., Sarradin P. M., Cathalot C. and Riso R. D. (2015) A comparison of in situ vs. ex situ filtration methods on the assessment of dissolved and particulate metals at hydrothermal vents. *Deep Sea Res. I.* **105**, 186–194.
- Daskalakis K. D. and Helz G. R. (1993) The solubility of sphalerite (ZnS) in sulfidic solutions at 25C and 1 atm pressure. *Geochim. Cosmochim. Acta.* **57**, 4923–4931.
- Degens E. T., Okada H., Honjo S. and Hathaway J. C. (1972) Microcrystalline Sphalerite in Resin Globules Suspended in Lake Kivu, East Africa. *Mineral. Deposita* **7**, 1–12.
- Drummond S. E. and Ohmoto H. (1985) Chemical evolution and mineral deposition in boiling hydrothermal systems. *Econ. Geol. Bull. Soc. Econ. Geol.* **80**, 126–147.
- Edmond J. M., Von Damm K. L., McDuff R. E. and Measures C. I. (1982) Chemistry of hot springs on the East Pacific Rise and their effluent dispersal. *Nature* **297**, 187–191.
- Farquhar J., Johnston D. T., Wing B. A., Habicht K. S., Canfield D. E., Airieau S. and Thiemens M. H. (2003) Multiple Sulphur isotopic interpretations of biosynthetic pathways: implications for biological signatures in the sulphur isotope record. *Geobiology* **1**, 27–36.
- Feely R. A., Geiselman T. L., Baker E. T. and Massoth G. W. (1990) Distribution and Composition of Hydrothermal Plume Particles From the ASHES Vent Field at Axial Volcano, Juan de Fuca Ridge. *J. Geophys. Res.* **95**, 12855–12873.
- Feely R. A., Lewison M., Massoth G. J., Robert-Baldo G., Lavelle J. W., Byrne R. H., Von Damm K. L. and Curl, Jr., H. C. (1987) Composition and dissolution of black smoker particulates from active vents on the Juan De Fuca ridge. *J. Geophys. Res.* **92**, 11347–11363.
- Findlay A. J., Gartman A., MacDonald D. J., Hanson T. E., Shaw T. J. and Luther, III, G. W. (2014) Distribution and size fractionation of elemental sulfur in aqueous environments: the Chesapeake Bay and Mid-Atlantic Ridge. *Geochim. Cosmochim. Acta.* **142**, 334–348.
- Findlay A. J., Gartman A., Shaw T. J. and Luther, III, G. W. (2015) Trace metal concentration and partitioning in the first 1.5 m of hydrothermal plumes along the Mid-Atlantic Ridge: TAG Snakepit and Rainbow. *Chem. Geol.* **412**, 117–131.
- Findlay A. J., Estes E. R., Gartman A., Yücel M., Kamyshtny A. and Luther, III, G. W. (2019) Iron and sulfide nanoparticle formation and transport in nascent hydrothermal vent plumes. *Nat. Geosci.* **10**, 1597.
- Fitzsimmons J. N., John S. G., Marsay C. M., Hoffman C. L., Nicholas S. L., Toner B. M., German C. R. and Sherrell R. M. (2017) Iron persistence in a distal hydrothermal plume supported by dissolved-particulate exchange. *Nat. Geosci.* **10**, 195–201.
- Foustoukos D. I. and Seyfried, Jr., W. E. (2007) Fluid phase separation processes in submarine hydrothermal systems. *Rev. Mineral. Geochem.* **65**, 213–239.
- Gamo T., Ishibashi J., Tsunogai U., Okamura K. and Chiba H. (2006) Unique geochemistry of submarine hydrothermal fluids from arc-back-arc settings of the western pacific. In *Back-Arc Spreading Systems: Geological, Biological, Chemical, and Physical Interactions*, vol. 166 (eds. D. M. Christie, C. R. Fisher, S.-M. Lee and S. Givens). AGU Monograph. American Geophysical Union, pp. 147–161.
- Garbe-Schönberg D. (1993) Simultaneous determination of thirty-seven elements in twenty eight international rock standards by ICP-MS. *Geostandard. Newslett.* **17**, 81–97.
- Gardner G. L. and Nancollas G. H. (1983) Crystal growth in aqueous solution at elevated temperatures. Barium sulfate growth kinetics. *J. Phys. Chem.* **87**, 4699–4703.
- Gartman A., Findlay A. J. and Luther, III, G. W. (2014) Nanoparticulate pyrite and other nanoparticles are a widespread component of hydrothermal vent black smoker emissions. *Chem. Geol.* **366**, 32–41. <https://doi.org/10.1016/j.chemgeo.2013.12.013>.
- Gartman A., Picard A., Olins H. C., Sarode N., Clarke D. R. and Girguis P. R. (2017) Microbes facilitate mineral deposition in bioelectrochemical systems. *ACS Earth Space Chem.* **1**, 277–287.
- Gartman A., Hannington M., Jamieson J. W., Peterkin B., Garbe-Schönberg D., Findlay A. J., Fuchs S. and Kwasnitschka T. (2018) Boiling-induced formation of colloidal gold in black smoker hydrothermal fluids. *Geology* **46**, 39–42.
- Hannington M. D. and Garbe-Schönberg D. (2019) Detection of gold nanoparticles in hydrothermal fluids. *Econ. Geol.* **114**, 397–400.
- Hawkes J. A., Rossel P. E., Stubbins A., Butterfield D., Connelly D. P., Achterberg E. P., Koschinsky A., Chavagnac V., Hansen C. T., Bach W. and Dittmar T. (2015) Efficient removal of recalcitrant deep-ocean dissolved organic matter during hydrothermal circulation. *Nat. Geosci.* **8**, 856–850.
- Haymon R. M. and Kastner M. (1981) Hot spring deposits on the East Pacific Rise at 21°N preliminary description of mineralogy and genesis. *Earth. Planet. Sci. Lett.* **53**, 363–381.
- Hein J. R., Mizell K. and Barnard P. L. (2013) Sand sources and transport pathways for the San Francisco Bay coastal system, based on X-ray diffraction mineralogy. *Mar. Geol.* **345**, 154–169.
- Hochella M. F., Lower S. K., Maurice P. A., Penn R. L., Sahai N., Sparks D. L. and Twining B. S. (2008) Nanominerals, mineral nanoparticles, and earth systems. *Science* **319**, 1631–1635.
- Hochella M. F., Aruguete D., Kim B. and Madden A. S. (2012) Naturally occurring inorganic nanoparticles: general assessment and a global budget for one of earth's last unexplored major geochemical components. In *Nature's Nanostructures*

- (eds. A. S. Barnard and H. Guo). Pan Stanford Publishing, Singapore, pp. 1–42.
- Hsu-Kim H., Mullaugh K. M., Tsang J. J., Yücel M. and Luther, III, G. W. (2008) Formation of Zn- and Fe-sulfides near hydrothermal vents at the Eastern Lau Spreading Center: implications for sulfide bioavailability to chemoautotrophs. *Geochim. Trans.* **9**, 6.
- Huang F., Zhang H. and Banfield J. F. (2003) Two-stage crystal-growth kinetics observed during hydrothermal coarsening of nanocrystalline ZnS. *Nano Lett.* **3**, 373–378.
- Jankowski P. (2011) *NI 43-101 Technical Report 2011 PNG, Tonga, Fiji, Solomon Islands, New Zealand, Vanuatu and the ISA*. SRK Consulting Pty Ltd.
- Jamieson J. W., Hannington M. D., Tivey M. K., Hansteen T., Williamson N. M., Steward M., Fietzke J., Butterfield D., Frische M., Allen L., Cousens B. and Langer J. (2016) Precipitation and growth of barite within hydrothermal vent deposits from the Endeavour Segment, Juan de Fuca Ridge. *Geochim. Cosmochim. Acta* **173**, 64–85.
- James R. H. and Elderfield H. (1996) Chemistry of ore-forming fluids and mineral formation rates in an active hydrothermal sulfide deposit on the Mid-Atlantic Ridge. *Geology* **24**, 1147–1150.
- Kamyshtny A., Druschel G., Mansaray Z. F. and Farquhar J. (2014) Multiple sulfur isotopes fractionations associated with abiotic sulfur transformations in Yellowstone National Park geothermal springs. *Geochim. Trans.* **15**, 7.
- Kleint C., Hawkes J. A., Sander S. G. and Koschinsky A. (2016) Voltammetric investigation of hydrothermal iron speciation. *Front. Mar. Sci.* **3**, 1–11.
- Klevenz V., Bach W., Schmidt K., Hentscher M., Koschinsky A. and Petersen S. (2011) Geochemistry of vent fluid particles formed during initial hydrothermal fluid-seawater mixing along the Mid-Atlantic Ridge. *Geochim. Geophys. Geosyst.* **12**, 1–23.
- Koschinsky A., Garbe-Schönberg D., Sander S., Schmidt K., Gennerich H. and Strauss H. (2008) Hydrothermal venting at pressure-temperature conditions above the critical point of seawater, 5°S on the Mid-Atlantic Ridge. *Geology* **36**, 615–618.
- Kwasnitschka T., Köser K., Duda A., Jamieson J. W., Boschen R., Gartman A., Hannington M. D. and Fungaitao C. (2016) Virtual Vents: A microbathymetrical survey of the Niuia South Hydrothermal Field, NE Lau Basin, Tonga. American Geophysical Union Fall Meeting, San Francisco, USA, #OS43D-06 (abstr.).
- Lupton J., Rubin K. H., Arculus R., Lilley M., Butterfield D., Resing J., Baker E. and Embley R. (2015) Helium isotope, C/³He, and Ba-Nb-Ti signatures in the northern Lau Basin: distinguishing arc, back-arc, and hotspot affinities. *Geochim. Geophys. Geosyst.* **16**, 1133–1155.
- McDermott J. M., Ono S., Tivey M. K., Seewald J. S., Shanks W. C. I. I. and Solow A. R. (2015) Identification of sulfur sources and isotopic equilibria in submarine hot-springs using multiple sulfur isotopes. *Geochim. Cosmochim. Acta* **160**, 169–187.
- Metz S. and Trefry J. H. (2000) Chemical and mineralogical influence on concentrations of trace metals in hydrothermal fluids. *Geochim. Cosmochim. Acta* **64**, 2267–2279.
- Monecke T., Petersen S. and Hannington M. D. (2014) Constraints on water depth of massive sulfide formation: Evidence from modern seafloor hydrothermal systems in Arc-Related settings. *Econ. Geol.* **109**, 2079–2101.
- Monecke T., Petersen S., Hannington M. D., Grant H. and Samson I. (2016) The minor element endowment of modern sea-floor massive Sul des and comparison with deposits hosted in ancient volcanic successions. *Rev. Econ. Geol.* **18**, 245–306.
- Nakamura R., Takashima T., Kato S., Takai K., Yamamoto M. and Hashimoto K. (2010) Electrical current generation across a black smoker chimney. *Angew. Chem.* **122**, 7858–7860.
- Ono S., Wing B., Johnston D., Farquhar J. and Rumble D. (2006) Mass-dependent fractionation of quadruple stable sulfur isotope system as a new tracer of sulfur biogeochemical cycles. *Geochim. Cosmochim. Acta* **70**, 2238–2252.
- Ono S., Shanks, III, W. C., Rouxel O. J. and Rumble D. (2007) S-33 constraints on the seawater sulfate contributions in modern seafloor hydrothermal vent sulfides. *Geochim. Cosmochim. Acta* **71**, 1170–1182.
- Peterkin B., Jamieson J. W., Kwasnitschka T. and Hannington M. D. (2018) Formation of hydrothermal sulfide deposits on the Niuia South Volcano, Northeast Lau Basin. Resources for Future Generations Conference, Vancouver, Canada (abstr.).
- Reich M., Utsunomiya S., Kesler S. E., Wang L., Ewing R. C. and Becker U. (2006) Thermal behavior of metal nanoparticles in geologic materials. *Geology* **34**, 1033–1036.
- Resing J., Embley R., Merle S., and Shipboard Scientific Party (2012) Submarine Ring of Fire-2012 (SRoF-12) Northeast Lau Basin: R/V Roger Revelle Expedition RR12111, Cruise Report Sept 9–25, 2012, Suva-Samoa, 260 p.
- Resing J. A., Sedwick P. N., German C. R., Jenkins W. J., Moffett J. W., Sohst B. M. and Tagliabue A. (2015) Basin-scale transport of hydrothermal dissolved metals across the South Pacific Ocean. *Nature* **523**, 200–203.
- Reynolds G. T. and Lutz R. A. (2001) Sources of light in the deep ocean. *Rev. Geophys.* **39**, 123–136.
- Rouxel O., Toner B. M., Manganini S. J. and German C. R. (2016) Geochemistry and iron isotope systematics of hydrothermal plume fall-out at East Pacific Rise 9°50'N. *Chem. Geol.* **441**, 212–234.
- Russel W., Saville D. and Schowalter W. (1989) *Colloidal Dispersions (Cambridge Monographs on Mechanics)*. Cambridge University Press, Cambridge.
- Sander S. G. and Koschinsky A. (2011) Metal flux from hydrothermal vents increased by organic complexation. *Nat. Geosci.* **4**, 145–150.
- Scherrer P. (1918) Bestimmung der Größe und der inner Struktur von Kolloidteilchen mittels Röntgenstrahlen Göttinger Nachrichten. *Math. Phys.* **2**, 98–100.
- Schmidt K., Koschinsky A., Garbe-Schönberg D., de Carvalho L. M. and Seifert R. (2007) Geochemistry of hydrothermal fluids from the ultramafic-hosted Logatchev hydrothermal field, 15°N on the Mid-Atlantic Ridge: temporal and spatial investigation. *Chem. Geol.* **242**, 1–21.
- Schmidt K., Garbe-Schönberg D., Hannington M. D., Anderson M. O., Bühring B., Haase K., Haruel C., Lupton J. and Koschinsky A. (2017) Boiling vapour-type fluids from the Nifonea vent field (New Hebrides Back-Arc, Vanuatu, SW Pacific): geochemistry of an early-stage, post-eruptive hydrothermal system. *Geochim. Cosmochim. Acta* **207**, 185–209.
- Seyfried, Jr., W. E. and Ding K. (1993) The effect of redox on the relative solubilities of copper and iron in Cl-bearing aqueous fluids at elevated temperatures and pressures: an experimental study with application to seafloor hydrothermal systems. *Geochim. Cosmochim. Acta* **57**, 1905–1917.
- Sharma V., Park K. and Srinivasarao M. (2009) Colloidal dispersion of gold nanorods: historical background, optical properties, seed-mediated synthesis, shape separation and self-assembly. *Mater. Sci. Eng. R Rep.* **65**, 1–38.
- Steefel C. I. and Van Cappellen P. (1990) A new kinetic approach to modeling water-rock interaction: the role of nucleation,

- precursors, and Ostwald ripening. *Geochim. Cosmochim. Acta*. **54**, 2657–2677.
- Stoffers P., Worthington T. J., Schwarz-Schampera U., Hannington M. D., Massoth G. J., Hekinian R., Schmidt M., Lundsten L. J., Evans L. J., Vaionio'unga R. and Kerby T. (2006) Submarine volcanoes and high-temperature hydrothermal venting on the Tonga arc, southwest Pacific. *Geology* **34**, 453–456.
- Tivey M. K., Bradley A. M., Joyce T. M. and Kadko D. (2002) Insights into tide-related variability at seafloor hydrothermal vents from time-series temperature measurements. *Earth Planet. Sci. Lett.* **202**, 693–707.
- Tohver V., Smay J. E., Braem A., Braun P. V. and Lewis J. A. (2001) Nanoparticle halos: a new colloid stabilization mechanism. *Proc. Natl. Acad. Sci.* **98**, 8950–8954.
- Toner B. M., Fakra S. C., Manganini S. J., Santelli C. M., Marcus M. A., Moffett J. W., Rouxel O., German C. R. and Edwards K. J. (2009) Preservation of iron(II) by carbon-rich matrices in a hydrothermal plume. *Nat. Geosci.* **2**, 197–201.
- Toner B. M., Berquó T. S., Michel F. M., Sorensen J. V., Templeton A. S. and Edwards K. J. (2012) Mineralogy of iron microbial mats from Loihi Seamount. *Front. Microbiol.* **3**, 1–18.
- Toner B. M., German C. R., Dick G. J. and Breier J. A. (2016) Deciphering the complex chemistry of deep-ocean particles using complementary synchrotron X-ray microscope and microprobe instruments. *Acc. Chem. Res.* **49**, 128–137.
- Tooth B., Ciobanu C. L., Green L., O'Neill B. and Brugger J. (2011) Bi-melt formation and gold scavenging from hydrothermal fluids: an experimental study. *Geochim. Cosmochim. Acta*. **75**, 5423–5443.
- Törmänen T. A. and Koski R. A. (2006) Gold enrichment and the Bi-Au association in pyrrhotite-rich massive sulfide deposits, Escanaba Trough, Southern Gorda Ridge. *Econ. Geol. Bull. Soc. Econ. Geol.* **100**, 1135–1150.
- Vogel W., Borse P. H., Deshmukh N. and Kulkarni S. K. (2000) Structure and stability of monodisperse 1.4-nm ZnS particles stabilized by mercaptoethanol. *Langmuir* **16**, 2032–2037.
- White S. N., Chave A. D. and Reynolds G. T. (2002) Investigations of ambient light emission at deep-sea hydrothermal vents. *J. Geophys. Res.* **107**, B1.
- Yücel M., Gartman A., Chan C. S. and Luther, III, G. W. (2011) Hydrothermal vents as a kinetically stable source of iron-sulphide-bearing nanoparticles to the ocean. *Nat. Geosci.* **4**, 367–371.
- Zhang G., Wang W., Lu X. and Li X. (2008) Solvothermal synthesis of V-VI binary and ternary hexagonal platelets: the oriented attachment mechanism. *Cryst. Growth Des.* **9**, 145–150.
- Zhen-Wu B. Y., Dideriksen K., Olsson J., Raahauge P. J., Stipp S. L. S. and Oelkers E. H. (2016) Experimental determination of barite dissolution and precipitation rates as a function of temperature and aqueous fluid composition. *Geochim. Cosmochim. Acta*. **194**, 193–210.

Associate editor: Jun-ichiro Ishibashi